

Context depenedent localisation of short term memory.

Jingjie Li^{1,2,3,4}, Chaofei Bao^{1,2,3,4}, Albert Albesa-González⁵, Ariel Ziqian Xu¹, Liujunli Li^{2,3,4}, Claudia Clopath^{1,5}, Jeffrey C. Erlich^{1,2,3,4*}

1 Sainsbury Wellcome Centre, University College London, London, UK

2 NYU-ECNU Institute of Brain and Cognitive Science at NYU Shanghai, China

3 NYU Shanghai, Shanghai, China

4 Shanghai Key Laboratory of Brain Functional Genomics (Ministry of Education),
East China Normal University, Shanghai, China

5 Imperial College London, London, UK

*Correspondence to: j.erlich at ucl.ac.uk

The authors have no conflict of interest nor financial interests.

Abbreviated Title: Context dependent localisation of short term memory.

Figures: 6

Tables: 0

Supplemental Material: 8 Figures, X tables

Number of words in

Abstract: XX

Introduction: XX

Results: XX

Methods: XX

Discussion: XX

¹ Abstract

² Movement planning involves multiple coordinate systems^{1–4}, but this is complexity is
³ missing from simple go/no-go or 2-choice tasks^{5–8}. Using a 7-port wall⁹, we trained
⁴ rats on two memory-guided tasks, varying start position across trials. One task mapped
⁵ sounds to egocentric directions (e.g. turn left), the other to allocentric locations (e.g. go
⁶ to port A). Frontal cortical activity predicted choice and was necessary in the egocentric
⁷ task, but not the allocentric one. We hypothesized that the frontal cortex supports
⁸ planning only when an egocentric strategy is used, and that in the allocentric task, rats
⁹ instead remembered the sound or location to avoid the high memory cost of maintaining
¹⁰ directions across changing start positions. Specifically, solving the allocentric task in self-
¹¹ centered coordinates required remembering one of 12 possible movement vectors from
¹² start to location (3.6 bits). But, solving it in a sound- or location-based frame required
¹³ storing only a single bit. A dynamical model implementing this cost-sensitive strategy-
¹⁴ selection recapitulated our results and predicted that simplifying the allocentric task to
¹⁵ a single start position would cause animals to revert to an egocentric strategy. Indeed,
¹⁶ the simplified task rapidly became dependent on frontal cortex. These findings reveal
¹⁷ flexible, cost-sensitive selection of mnemonic strategies¹⁰ and suggest the frontal cortex
¹⁸ is specialized for planning in self-centered coordinates.

¹⁹ Introduction

²⁰ Movement planning in real-life contexts is complex. When asking for directions to
²¹ the nearest pharmacy you may receive instructions in self-centered coordinates—‘Go two
²² blocks and then turn left and go another 3 blocks’—or in world-centered coordinates—
²³ ‘there is one at the corner of Wells and Lake’. However, there are many open ques-
²⁴ tions about the shared and distinct neural mechanisms of these two forms of planning.
²⁵ There has been substantial focus on self-centered movement planning, especially for eye-
²⁶ movements¹¹ or reaches^{12–14} in monkeys, and head-orientation⁵ or licking¹⁵ in rodents,
²⁷ across the frontal-parietal-tectal network^{7–9,16}, including self-centered coordinate trans-
²⁸ formations (e.g. eye-hand, eye-head)^{2,17,18}. These studies often require animals to be
²⁹ under tight experimental control: i.e., maintain fixation during planning.

³⁰ Separately, there has been extensive exploration of allocentric representations in the
³¹ hippocampus and entorhinal cortex¹⁹, but not as much on planning *per se*^{20,21}. Mixing
³² of allocentric and egocentric representations have also been found in frontal^{4,9,22}, pari-
³³ etal^{23,24}, and entorhinal²⁵ cortices. These studies often involve relatively unconstrained
³⁴ behavior with animals moving freely in a maze or open field. Thus, there is a gap in
³⁵ the literature where animals under tight experimental control are given instructions in
³⁶ an allocentric reference frame.

³⁷ Moreover, real-life tasks often involve delays, where one must complete the current
³⁸ step or wait before executing the next planned movement. In delayed-response tasks,
³⁹ the secondary motor cortex (M2) and related areas^{5,6,15,26,27} have been well studied for
⁴⁰ their roles in maintaining information and planning upcoming movements during short
⁴¹ delays. However, these studies typically rely on relatively simple two-alternative forced-
⁴² choice (2AFC) tasks, where animals orient to either the left or right port or lick left/right
⁴³ spouts to make choices. For 2AFC tasks, the consensus view is that M2 instantiates
⁴⁴ a bi-stable attractor for planning upcoming choices^{6,26,28,29}. However, the reductionist
⁴⁵ nature of these tasks precludes us from understanding what ‘planning activity’ in M2

46 represents. Are these representations encoding egocentric plans (upcoming movement
47 direction), allocentric goals (upcoming target position), or abstract labels³⁰?

48 We began to address this in Li et al.,⁹ by examining the representations in a visually-
49 guided movement planning task in rats, where movements were made from different start
50 positions along several movement directions. We found that in the frontal orienting field
51 (FOF) in M2, planning was in self-centered coordinates. However, we also found repre-
52 sentations of the current position of the rat. Since the target locations were indicated
53 with visual cues, the task instructions were inherently self-centered. If instructions are
54 provided in an allocentric frame, does the FOF still serve as the substrate for planning?
55 Can the FOF plan in allocentric coordinates?

56 To address these questions, we designed a pair of novel auditory memory-guided
57 orienting tasks. In the ‘Ego’ task, the sound cues were linked to movement direction.
58 In the ‘Allo’ task, the sound cues were linked to target position. In both tasks, the
59 current position of the rat could be reliably decoded⁹. However, both electrophysi-
60 logical and optogenetic evidence revealed a dramatic shift in the neural mechanisms
61 supporting planning between these tasks. In the Ego task, the upcoming choice could be
62 decoded from FOF activity and silencing the FOF during the memory period impaired
63 performance. Moreover, planning activity for upcoming leftward/rightward movements
64 generalized across varying starting positions. In contrast, in the Allo task, we observed
65 no planning-related signals in the FOF and silencing had no significant effect.

66 Furthermore, the FOF is rapidly re-engaged in the Allo animals after simplifying the
67 task to encourage a self-centered strategy. This demonstrated that the FOF could be
68 quickly re-recruited following changes in the reference frame structure of a movement
69 planning task. We propose that the role of M2 (FOF) in planning is not universal.
70 Rather, the FOF is the neural substrate for self-centered movement plans. This is the
71 preferred representation for planning, but in cases where the task makes this represen-
72 tation inefficient, animals can shift mnemonic strategies to one that is more efficient.

73 Results

74 Two auditory memory-guided tasks in different reference frames

75 We separately trained two groups of rats on either the Ego or the Allo task (details
76 of subjects can be found in Table 1). The Ego and Allo tasks followed the exact same
77 temporal structure. Each trial started with the illumination of a randomly selected start
78 poke. Rats needed to poke into the start port and remain fixated their nose in start
79 port for 1.5s, rats experienced a 0.75s sound cue followed by another 0.75s delay period.
80 An auditory ‘go’ cue signalled the beginning of the choice period, rat reported sound
81 cue by poking into the target port (Figure 1a).

82 The target port was defined based on task context and start port. For the Ego
83 task variation, the left/right adjacent port of the start port could be the correct tar-
84 get port for sound cue blue/red, respectively(Figure 1c, left). Since the correct tar-
85 get port could move together with the start port for each trial, we described it as an
86 egocentric task. This yields 8 different trial-types with 2 different moving direction
87 vectors(Supplementary Figure 1a, left panel). For the Allo task variation, the bottom
88 left/bottom right port in the wall could be the correct target port for sound cue blue/red,
89 respectively(Figure 1b, right). Since the correct target port was fixed in the physical
90 space, we described it as an allocentric task. This yields 12 different trial-types with 10
91 different moving direction vectors(Supplementary Figure 1a, right panel).

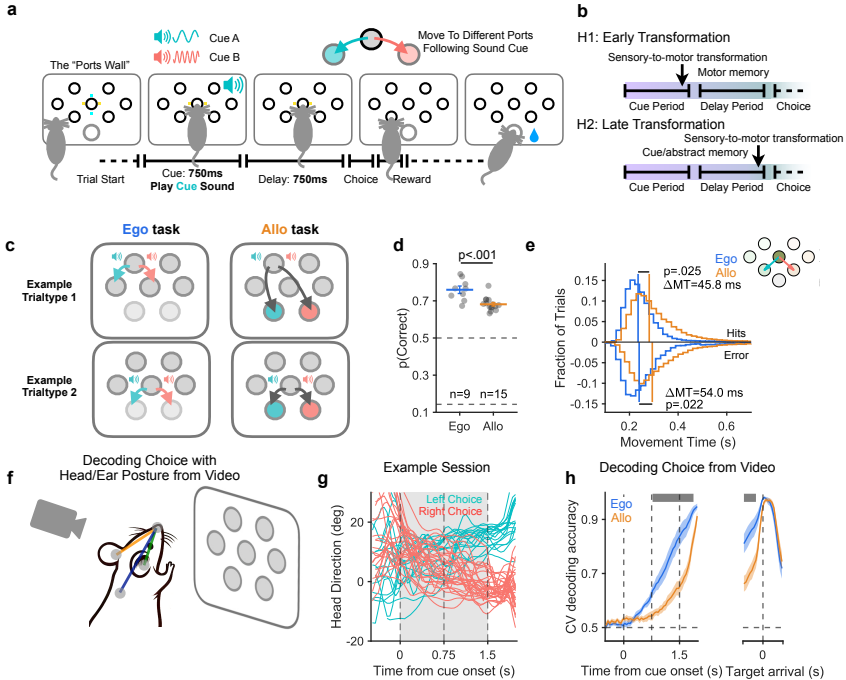


Figure 1. Task design and behavior quantification **a.** Schematic of the task. **b.** The task can be solved by performing an early sensory-motor transform and remembering a prospective motor-plan during the delay (H1) or by remembering a retrospective cue/category memory and performing a late sensory-motor transform. **c.** Mapping the sounds to the ports in the two tasks. For the Ego task, the sounds mapped to ports relative to start port. For the Allo task, the sounds mapped to fixed ports. **d.** Performance. Grey dots are for individual rats and the line indicates mean for each task. **e.** Movement time (MT) distribution for the Ego task and the Allo task, for center-port started trials. Histograms of MT from Ego and Allo tasks are shown here for hits (Top) and error (Bottom) trials. Vertical line: median of RT. **f.** Example key points and vector angles feature for video decoding analysis: Nose, Left/Right Ear, Neck, and vectors between those key points. **g.** Head direction trajectory from one example session. Each thin line are for a trial. The grey box highlighted the fixation period when the rat held their nose in the start port before making a choice. **h.** Averaged decoding accuracy for choice from posture features at each time point. Shaded: SEM across subjects. The thick grey bar at the top indicates the time when the decoding accuracy was significantly different on the ego verse allo task($p < .05$, two-sample t-test with FDR correction).

92 Rats can perform both tasks well. Rats well understood the task structure for both
93 tasks: most of the error choices were made to the choice port corresponding to the
94 opposite sound cue (ego task: 94.9%, allo task: 94.7%, see Supplementary Figure 1b).
95 On average, the hit rate for rats performed the allo task was $0.681 \pm 0.009\%$ S.E. (n=15
96 rats, 1329 sessions, 279,676 trials) and for the ego task, it was $0.759 \pm 0.020\%$ S.E. (n=9
97 rats, 506 sessions, 85,597 trials) after the removal of all broken fixation trials and timeout
98 trials (Figure 1d). The hit rate of both tasks exceeded two chance levels (0.5 if animals
99 don't distinguish the binary cue or, 0.14 if animals choose the 1/7 choice port randomly).
100 The hit rate of rats doing the Ego task is significantly higher than the allo task ($p < .001$,
101 $t = 4.168$, two-sampled t-test).

102 In classic delayed-response tasks, evidence of movement planning after a sensory-to-
103 motor transformation can be reflected in behavioral levels: faster movement time (MT)
104 and small posture adjustment during the delay period toward the target^{5,31}. In our
105 two task designs, trials started from the center port are identical under two task varia-
106 tions. We use those same-movement trials to analysis for movement time and posture
107 adjustment for choice. To assess whether movement time (MT) distributions differed
108 between the allo and ego task, we fit a generalized linear mixed model (GLMM) with
109 task condition as a fixed effect and subject identity as a random effect. A correspondingly
110 reduced model, excluding the task term, was used for comparison. We then performed
111 a likelihood ratio test (LRT) to evaluate whether task condition significantly accounted
112 for variance in MT.

113 For the movement time, we found that the time from exiting the center port until
114 reaching the chosen port was, on average, 45.9 ms shorter on the ego task trials compared
115 with the allo task (Figure 1e, Ego task: median MT = 235.4ms (234.4ms to 236.5ms,
116 95% C.I.), n=17,889 trials Allo task: median MT = 281.3ms (280.2ms to 282.3ms, 95%
117 C.I.) n=37,561 trials, $p=.019$, LRT). From error trials, we observed the same amount of
118 difference (Ego task: median MT = 239.8ms (237.5ms to 242.0ms, 95% C.I.), n=7,380
119 trials Allo task: median MT = 293.8ms (291.6ms to 295.6ms, 95% C.I.) n=17,214 trials,
120 $p=.020$, LRT). This result is consistent with the slower RT/MT without delay period^{5,32}
121 or with an extra step of internal conversion³³ in previous literature.

122 Movement planning during the delay period could come with uninstructed move-
123 ment^{5,31,34}. We compared the choice-related uninstructed movement in two task vari-
124 ations. With SLEAP³⁵, we extracted several key-points from the video and further
125 extracted the vector between those key points (Figure 1f). Intuitively, rat will tend to
126 gradually and slightly turn their heads toward their intended target before they are al-
127 lowed to move in order to get prepared for a faster move. We plotted the head direction
128 vector as a function of the time aligned to the onset of the trial, colored by different
129 choice for an example session (Figure 1g). As can be seen from the plot, when the rat
130 kept its nose inside the start port during cue period and delay period (highlighted by the
131 grey area), two groups of lines started to be separated clearly progressively. To quan-
132 tify this separation of body movement for up-coming choice. We furthermore trained
133 a linear classifier that take the angle between keypoints pairs at each timepoint in the
134 trial to predict rats' choice, with center port started trials only. For each timepoint,
135 we quantified the decoding accuracy for each rat and plotted it against time. We found
136 that, on average, we were able to decode choice from rats' posture during the delay
137 period and early movement period better in the ego task compared with the allo task
138 (Figure 1h, left panel). As a control, before rats reached the target port we were able
139 to decode their choice at perfect level (Figure 1h, right panel), which validated the ac-
140 curacy and precision of our decoding method from video. The difference of MT and

141 posture adjustment cannot be explained by outlier rats(Supplementary Figure 1c,d) nor
142 different performance level (Supplementary Figure 1e).

143 **FOF neurons encode start port similarly for two tasks, but not the same**
144 **for future choice**

145 Neurons in the FOF are known to maintain differentiated activity for different choices in
146 a simple delayed-response task⁵, contributing to short-term memory. In a more complex
147 orienting-planning task, FOF neurons encode both self-centered movement plans and
148 world-centered target positions⁹.

149 Building on these findings, the FOF could serve as a hub for maintaining short-term
150 memory for choice in our ego and allo task. To investigate this possibility, we recorded
151 single-unit activity from the FOF in rats performing both Ego and Allo tasks (Ego task:
152 n = 2,887 neurons, 4 rats; Allo task: n = 3,325 neurons, 8 rats).

153 In our task design, rats initiated trials from different start ports and received a binary
154 auditory cue, signaling two potential movement directions (Ego task) or two target ports
155 (Allo task). Following cue offset (the delay period), the rats were required to retain
156 this information during a delay period. A straightforward solution for completing the
157 task would involve maintaining a binary representation of the upcoming choice. Note
158 that during the delay period, rats were fixating at the start port in both tasks. The
159 only difference between the two groups of animals was the mapping between the binary
160 auditory cue and the upcoming choice port. We therefore examined whether FOF single-
161 neuron activity during the delay period differed as a function of this task-dependent
162 choice port definition, under identical sensory input and fixation position.

163 FOF neurons in both tasks exhibited distinct tuning for binary choices (example
164 neuron: Figure 2a,e for the ego- and allo-centric tasks, respectively), start port positions
165 (Figure 2b,f), or a combination of both factors (Figure 2c,g). To quantify this, we
166 computed a selectivity index based on the difference in spike counts during the delay
167 period between binary-choice trial types: left vs. right movement choices in the ego-
168 centric task, and left vs. right port choices in the allo-centric task. We only selected
169 trials that rats choose the correct target port in this analysis (hit trials). The sign of
170 the selectivity index was determined relative to the recording hemisphere, with positive
171 values indicating a preference for choices ipsilateral to the recording site and negative
172 values indicating contralateral preference. Only neurons with a firing rate of at least 0.5
173 Hz during the delay period were included (ego task: n = 2,388 neurons; allo task: n =
174 3,034 neurons; see Methods for details).

175 In addition to the selectivity index for binary choices, we quantified a selectivity
176 index for start port position by measuring differences in spike counts between trials
177 where the rat started at the farthest left and right ports (as above, sign adjusted to
178 ipsi/contral-lateral relative to the decoding hemisphere), as predicted by a GLM model
179 for each neuron (see Methods for details). The joint distribution of these two selectivity
180 indices is presented as a 2D scatter plot for each task (Figure 2d, h). For this analysis,
181 we included both hit trials and in-task error trials, in which rats chose the port opposite
182 to the one indicated by the given auditory cue.

183 We found that a significantly greater proportion of neurons showed selectivity for the
184 upcoming choice in the Ego task compared to the Allo task (Ego task: 38%; Allo task:
185 3%; χ^2 , p < .001, Figure 2d, h, x-axis). Conversely, more neurons exhibited significant
186 selectivity for start port position in the Allo task compared to the Ego task (Ego task:
187 61%; Allo task: 75%; χ^2 , p < .001, Figure 2d, h, y-axis). Consistent differences between

188 the allo and ego task were also apparent when the same analysis was performed on
 189 each subject (Supplementary Figure 2).

190 Those results suggested a potential difference for up-coming choice coding in FOF
 neurons.

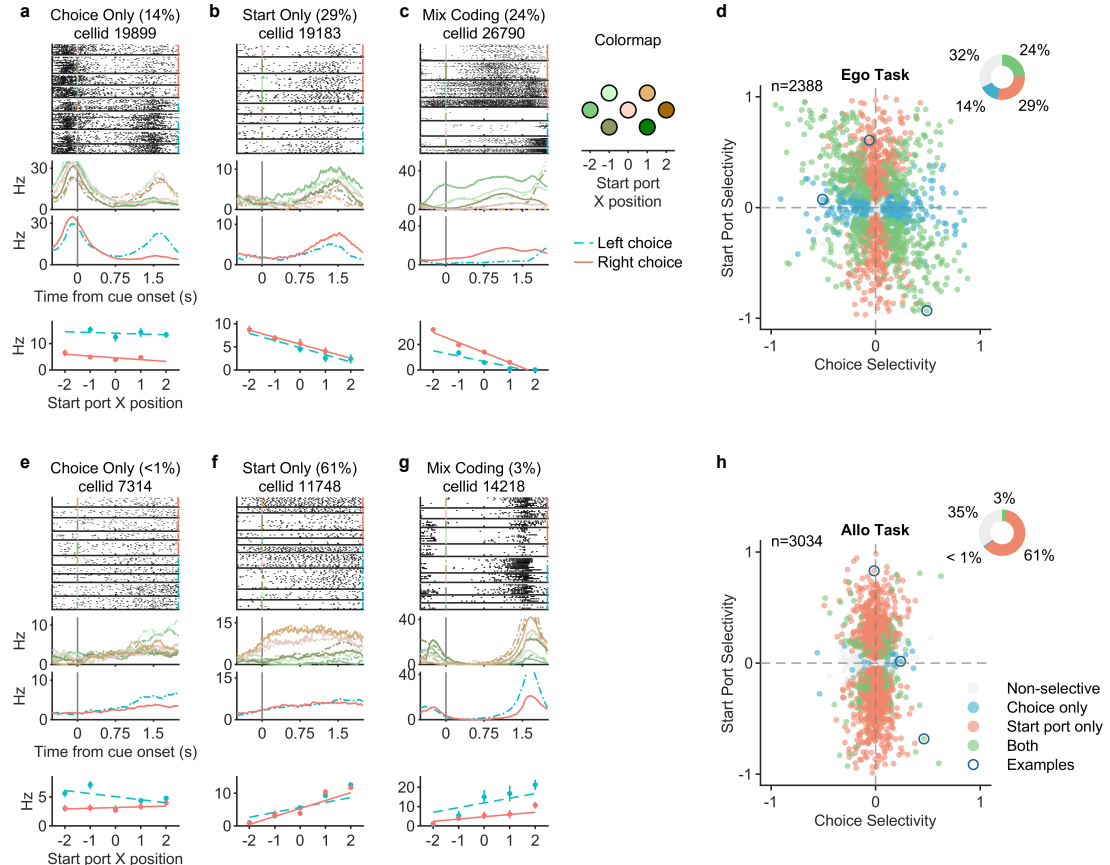


Figure 2. Single neuron quantification for choice and start port tuning **a-c** Example neurons from the Ego task. Spike raster plots and PSTHs of three representative neurons show heterogeneous dynamics during the fixation period. The rasters and PSTHs were aligned to the auditory cue onset and sorted by different start ports (indicated by different color) and upcoming choices (solid line for right choices, dashed line for left choices). The lower PSTH was sorted only on the basis of upcoming choices. The bottom row (firing rate versus start port position) summarizes the relationship among the neural activity, start port position and choice. The lines are fits of a linear model ($\text{Hz} \sim \text{start_port_posi} * \text{choice}$) to the data (dots with error bars represent mean \pm s.e.m.;). **d** Each point represents the choice (x-axis) and start (y-axis) selectivity of a single neuron in the Ego task. Blue, red, and green circles represent neurons with significant selectivity for choice, start or both. Black circled data show where the three example neurons shown in panel a-c are located in the scatter plot. **e-g.** same as panel a-c, but from the Allo task **h.** same as panel d, but from the Allo task.

191

192 Persistent and stable coding for egocentric choice in egocentric space 193 in FOF population

194 The single cell selectivity analysis revealed the potential difference between two tasks in
 195 FOF neurons. However, the selectivity analysis didn't control for different movement for
 196 different trialtypes. For example, in the allo task, for the trials started from the left side,
 197 rats will move rightward for both choice port, if the planning is for up-coming moving
 198 direction in egocentric space, grouping the trial based on choice port will underestimate

199 the encoding of FOF neurons. Moreover, taking the spike count during delay period
200 removed most of the temporal dynamics during the trial, which might also contribute
201 differently for two tasks.

202 To well control of different up-coming movement and also clarify the temporal dy-
203 namicm, in this part, we employ time-series analysis only focused on trials start from the
204 middle-center (MidC) port. For those trials, two tasks became identical for auditory cue,
205 timing, choice port and choice movement except the task context (Figure 3a, left conor).
206 For this analysis, we included both hit trials and in-task error trials, in which rats chose
207 the port opposite to the one indicated by the given auditory cue. We firstly counted the
208 percentage of neurons, out of the 2887 (Ego task), or 3225 (Allo task) recorded cells,
209 that had significantly different firing rates for left/right choices from MidC started trials,
210 and plotted this count as a function of time for each task. (Figure 3a). We observed a
211 persistently larger amount of neurons showing greater selectivity over the time-course
212 after the onset of delay period (χ^2 , $p < .001$).

213 However, motor cortex is known to encode upcoming movment in population space.
214 We employed pseudopopulation decoding to examine choice coding in population space,
215 as well as providing a better control for number of trials for each trialtypes. To generate
216 pseudopopulations, we pooled all the neurons across sessions where there were at least
217 10 trials for each left/right choices, from only MidC port started trials. This criteria
218 restricted our dataset to 2,339/2,935 neurons from 57/63 sessions for the ego and allo
219 task, respectively. To prevent a few neurons/trials in the population from dominating
220 the decoding, we randomly resampled the neurons and trials without replacement to
221 construct 100 pseudopopulations (see method for detail). We decoded left/right chocies
222 label using a logistic regression classifier and quantified the averaged decoding accuracy
223 at each time point. The decoding accuracy of the ego task ramped up fast over the time
224 course. Target decoding emerged early for the Ego task and kept higher than the allo
225 task over the entire trial (Figure 3b, $p < .01$, permutation test).

226 At single session level, we employed logistic classifier for left/right choices started
227 from MidC trials to extract the latency when the decoding accuracy exceed 0.7. Overall,
228 the decoding latency of the ego task emerged before the go cue (1.05 ± 0.04 secs S.E.,
229 $n=51$ sessions), which is much earlier than the allo task which on average emerged after
230 the go cue (1.66 ± 0.02 secs S.E., $n=55$ seessions, comparision: $p < .001$, permutation test).
231 We examined the stability of representations by training decoders at one time and then
232 testing them at other times for pseudopopulations of ego and allo task (Figure 3d).
233 We found that the decoding for choice in the ego task is stable across the entire delay
234 period (Figure 3d, left panel, within red square), but not above chance for the allo task
235 (Figure 3d, right panel, within red square).

236 The strong and stable choice coding in the ego task is consistant with previous finding
237 on the delayed-response task in M2^{5,36}. However, the absence of choice coding in the
238 allo task, especially when we are comparing for the exact same up-coming movement
239 started from MidC ports, is surprising.

240 One may argue that this difference of choice coding might be due to different record-
241 ing quality or probe targetting among two groups of rats. To clarify that point, we exam-
242 ined the coding of different start port positions in FOF from single cell and population
243 level. We quantified the coding of start port as the R^2 calcualted from the actual start
244 port position of each trial against predicted start port position from a linear model for
245 single neuron or population (Figure 3e). We quantified the percentage of neurons that
246 show significant start position prediction over time. Along the time course of a trial, we
247 observed presistantly more cells predicting the start position in the allo task than the

248 ego task (Figure 3f). Decoding performance for start position from the pseudopopulation
249 in the allo task was stable for the entire fixation period when animals are in the
250 start port, for the ego task, however, it was significantly lower than the allo task for
251 most of the time during early cue period and most of the delay period (Figure 3g, $p < .01$,
252 permutation test, FDR correction). Again, we examined the stability of representations
253 by doing the cross-time generalizations decoding for pseudopopulations of ego and allo
254 task for start positions (Figure 3h). Here We found that the decoding of start position
255 in the allo task is stable across the entire fixation period (Figure 3h, right panel, within
256 white square), however, in the ego task it only yield a very good decoding along diagonal,
257 and reached the best decoding during the middle of the fixation period(Figure 3h, left
258 panel). Therefore, the recorded FOF population for the allo task is more informative
259 and stable than the ego task for the information about start position, which answered
260 the concern about recording quality.

261 Having known clearly that neuron population in FOF in planning for choice in the
262 Ego task during delay period. Now we want to ask how the population code for choice
263 in the ego task. We want to ask when FOF is coding for future choice in egocentric or
264 allocentric reference frame. To be specific, if FOF is coding for planning in the egocen-
265 tric reference frame, we can have the same population pattern for different trialtypes
266 moving to the same direction (Figure 3i), otherwise, if the FOF is coding in the allocen-
267 tric reference frame, we could have the same population pattern for different trialtypes
268 moving to the same port location. We can simply test this by generalising the decoder
269 cross different trialtypes.

270 To visualize choice planning encoding at the population level, we analysed FOF
271 activity in an activity space, where each dimension corresponds to activity of one neuron.
272 We estimated a ‘coding direction’ (CD) along which activity maximally discriminated
273 future left/right choice at the delay period (Figure 3i, Methods). Projecting to the CD,
274 the FOF population activity for left/right choice from MidC started trials can be very
275 well seperated (Figure 3j) for the ego task. Using the CD from MidC start trials on trials
276 started from other port but moved to the same direction (leftward/rightward adjacent
277 port), FOF population activity can still be well seperated for the chocie (Figure 3l;
278 Supplementary Figure 4a) in the ego task. Suggesting an egocentric coding mechanism
279 in FOF in the ego task. However, consistent with the weak decoding accuracy for
280 choice(Figure 3b, orange curve), CD in the allo task failed to separate future left/right
281 choice for MidC started trials (Figure 3k). It also failed to be generalized to trials shared
282 the same target port for potential allocenctric planning mechanism (Figure 3m, left
283 panel; Supplementary Figure 4b, rule A), nor to trials shared the same moving direction
284 for potential egocentric planning mechanism (Figure 3m, right panel; Supplementary
285 Figure 4b, rule B).

286 To statistically verified the visualization from CD analysis, we trained a logistic
287 classifier using spike count during the delay period for all units of each session with
288 MidC-started trials, and used that decoder to predict other trials. For the ego task,
289 the decoding accuracy for leftward/rightward trials using the generalised decoder was
290 0.779 ± 0.129 S.D. (Figure 3n, $n=60$ sessions, $p < .001$, bootstraped vs. change level).
291 This result confirmed that in the Ego task, activity pattern in FOF is the same for
292 planning leftward/rightward movement at different start positions, which is an egocentric
293 mechanism of planning.

294 In the allo task, logistic classifier trained from MidC started left/right port chosen
295 trials failed to be generlised to other left/right port chosen trials that started from other
296 ports. The decoding accuracy for that generlisation was 0.510 ± 0.055 S.D. (Figure 3o

left panel, n=70 sessions, p=0.12, bootstraped vs. change level) Interestingly, when generalised the same classifier to predict animals' choice from other port but shared the same moving direction as MidC started bottom-left/right chosen trials (± 45 degree movement), the accuracy was 0.691 ± 0.190 S.D. which was above chance but with a large variance (Figure 3o right panel, n=70 sessions, p<.001, bootstraped vs. change level). Suggested that in the allo task, FOF population is planning in egocentric reference - the FOF was using similar activity patterns for different trials shared the same up-coming movement direction. The above chance decoding accuracy here was consistent with the above chance decoding accuracy in the pseudopopulation (Figure 3b) around 1.5s right before the end of the delay period.

FOF causally support short-term memory for the ego task, but not the allo task

Given different activity signatures in FOF between the two tasks, we then tried to compare and quantify the different causal roles of FOF in the two tasks. Technically, we expressed stGTACR2³⁷ in pyramidal neurons at bilateral FOF(Methods) and implanted tapered fiber at FOF to deliver laser. Moreover, a sham fiber was also implanted at the posterior part of the skull to provide habituation for laser and fiber tethering and sham control (Figure 4a left). Optogenetically, we silenced bilateral FOF by delivering 473nm blue laser (Figure 4a right) in randomized trials during cue period or delay epoch (Figure 4b).

We fit four pairs of mixed-effects generalized linear models (GLMMs) to quantify the impact of optogenetic inactivation during the cue and delay periods of the allo/ego task, separately. Each model compared the effects of FOF versus Sham laser flash. The fixed effects included laser condition (on/off), fiber location (FOF/Sham), and their interaction, while session identity was modeled as a random effect to account for session-by-session variability in behavioral performance. For each full model, we constructed a corresponding reduced model by removing the interaction term, allowing us to isolate the differential effect of laser in FOF versus Sham sessions.

Likelihood ratio tests (LRTs) comparing full and reduced models yielded four p-values, each testing whether laser flash had a different effect in FOF versus Sham sessions (Figure 4c,d). A significant result in this test indicates a causal influence of FOF inactivation on task performance.

To quantify effect size, we computed the session-wise difference in accuracy between laser-on and laser-off trials, $\Delta p(\text{Correct})$, for each condition. We then defined $OPTO_{FOF}$ as the difference in $\Delta p(\text{Correct})$ between FOF and Sham sessions for each experimental condition ($\Delta p(\text{Correct})_{Sham} - \Delta p(\text{Correct})_{FOF}$, for cue/delay period \times allo/ego task. Ego task: n=48/30 for Sham/FOF sessions, 4 rats; Allo task: n=40/29 for Sham/FOF sessions, 5 rats). Under the null hypothesis that the laser had only a nonspecific effect (e.g., distraction), $OPTO_{FOF}$ would be zero. A negative $OPTO_{FOF}$, in conjunction with a significant LRT p-value, would indicate a causal role of FOF in task execution in that task condition.

For cue period FOF silencing compared with Sham fiber laser delivery, the Difference between $\Delta p(\text{Correct})$ from the Sham/FOF session of the Ego task was weakly impaired for 0.0389 (p=.031, LRT) as well as the Allo task for 0.0251 (p=.045, LRT). However, delay period FOF silencing produced a larger performance impairment in the Ego task for 0.0640 (p=.002, LRT). Consistent with weak choice coding for the Allo task in FOF, we didn't observe significant performance impairment for delay period

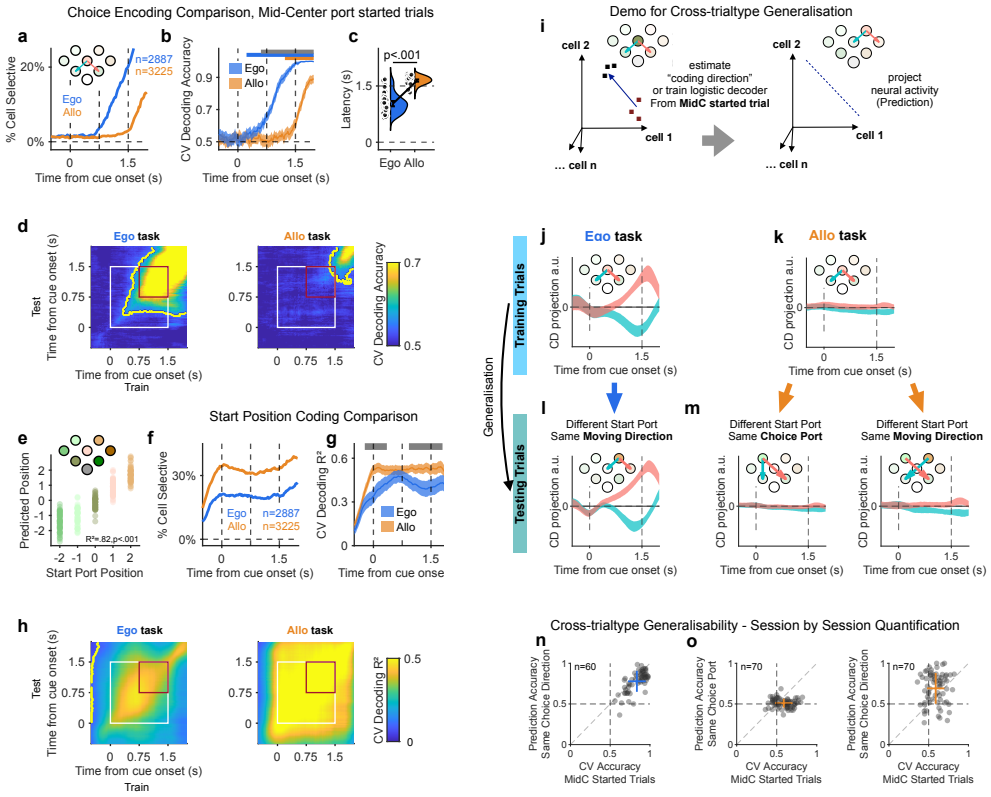


Figure 3. FOF population encoding of choice and start port information **a.** Development of choice-dependent activity over the time course of the trial. The lines indicate the % of cells that have significantly different firing rate for left/right choice from center port started trials. **b.** Averaged cross-validated decoding accuracy from 100 pseudo populations over the time course of the trial. Shaded indicate 99% C.I. The blue and orange thick bar at the top indicates the time when the decoding accuracy was significantly above chance for the Ego and Allo task. The grey bar indicates the time when the decoding accuracy was significantly different between the Ego vs. Allo task ($p < .01$, permutation test). **c.** Distribution of choice decoding latency of each session for choice. Dots are for each session. Errorbar indicated 99% C.I. **d.** Cross-validated choice decoding accuracy with cross-window decoding. Colors of the heat maps indicate the decoding accuracy for choice, averaged across 100 pseudopopulations. The decoders were trained at one time window (x-axis) and tested at another (y-axis). Contours, $p < 0.01$ (extreme pixel-based test). The white and red box highlight the fixation and delay period, respectively. **e.** Start port position decoding example session. Each dot indicates a trial. Performance was quantified as R^2 between actual and predicted position. **f.** Development of start port position dependent activity over the time course of the trial. **g.** Averaged decoding R^2 from 100 pseudo populations over the time course of the trial. Shaded indicate 99% C.I. The grey bar at the top indicates the time when the decoding accuracy was significantly different on the ego verse also task ($p < .01$, permutation test). **h.** Similar to textbf{d} but for start port decoding. **i.** illustration of cross-trialtype generalization for choice decoding. The Coding Direction (CD) or the decoder for left/right choices was trained with Mid-Center-started trials and was used to predict trials started from other ports. **j.** averaged activity trajectories (60 sessions) after Coding Direction (CD) projection on the correct left choice trials (blue) and right choice trials (red) from the Ego task. **k.** same as j for the Allo task. **l.** average activity trajectories (60 sessions) after CD projection on the correct left choice trials (blue) and right choice trials (red) from trials NOT started from MidC port from the Ego task. **m.** average activity trajectories (70 sessions) after CD projection on the correct left choice trials (blue) and right choice trials (red) from trials NOT started from MidC port from the Allo task (Left), or trials started from Top Left/right port that shared the same upcoming movement for the choice (Right). **n.** Decoding accuracy of MidC started trials against trials started from other start ports for each session (with generalised decoder from MidC trials). Cross indicates mean and S.D. of decoding accuracy of each axis. **o.** left: same as n for the Allo task. right: Decoding accuracy of MidC started trials against other trialtypes shared the same moving direction, for each session. Cross indicates mean and S.D. of decoding accuracy of each axis.

344 FOF silencing for the Allo task ($OPTO_{FOF}=0.0099$, $p=.214$, LRT). Thus, using this
345 metric, silencing FOF during the delay period significantly impaired the ego task but
346 not the allo task. Moreover, the FOF silencing effect was also observed at the individual
347 subject level(Supplementary Figure 5c,d) and session-wise (Supplementary Figure 5e,f).
348 However, comparing two groups to baseline is not the same as directly comparing them
349 to each other³⁸, so we turn to a more complex logistic mixed-effect model.

350 To sufficiently compare the difference in FOF silencing effect between the two tasks,
351 we designed a specific mixed-effect logistic model that considered performance fluctuation,
352 task baseline difference, visual effect of the laser, and most importantly, the
353 interaction between the two tasks and FOF silencing. By dropping the interaction term
354 and comparing the reduced model, we rigourously quantified the difference in the effect
355 of silencing FOF between the two tasks. We considered the cue period and the delay
356 period silencing seperately. For the cue period, we found no difference between the full
357 and reduced model, indicating that the effect of silencing was not significantly different
358 between the two tasks ($p=.569$, LRT). For delay period, there was a significant differ-
359 ence ($p=.005$, LRT). Thus, during the short-term memory period of the task (i.e. delay
360 period), the causal role of FOF was different across the two tasks. The summary of
361 $\Delta p(Correct)$ and details for sample size and statistics results were attached in table 3
362 and the statisitic appendix.

363 One potential confound is that the overall performance on the Allo task is worse
364 than the Ego task, which could make it hard to detect a significant effect of optogenetic
365 silencing of the FOF. To address that concern, ran the same analysis with a subset of
366 sessions from each task within the same range of performance (60 to 67 % correct). Even
367 in this subset of the data, the silencing FOF impaired Ego performance significantly more
368 than Allo performance ($p=.043$, Supplementary Figure 5h).

369 Another concern might be technical, perhaps we failed to get good expression or
370 misaligned the virus and optical fiber in the Allo task. checked the FOF silencing effect
371 for other aspects of the task for early withdraw rate (withdraw from the start port
372 before the end of fixation) and response time (RT, duration between the end of delay
373 period and the entry of choice port). Secondly, there was significantly slower RT and less
374 fixation early withdrawal with delay period FOF silencing for both tasks(Supplementary
375 Figure 6b,f). Those results suggested that FOF silencing produced a significant effect
376 on behavior, but just had different effects on animals' choice among the two tasks.

377 A dynamical model of cost-sensitive selection of working memory strat- 378 egy

379 We tried to use network modeling to explain the network architectures that support this
380 flexible recruitment of FOF for the delayed response task. It's known that the brain
381 have potentially different mechanism to support the short-term memory. For example,
382 the brain can use M2 networks for short-term memory for future movement^{5,15,26,27}, and
383 also other areas for short-term memory for the cue^{32,39-41}. Therefore, the goal here is
384 to explain the selection of different mechanisms based on different task demands for the
385 ego or allo task.

386 One important consideration was that the cost of maintaining a short-term mem-
387 ory in different systems (auditory/spatial-location/movement-planning) was different.
388 Which here we defined a 'memory cost per bits' for each memory system that stores the
389 given unit amount of information. We reasoned that the neural system will facilitate
390 the movement-planning(using FOF) as a default short-term memory mechanism (the

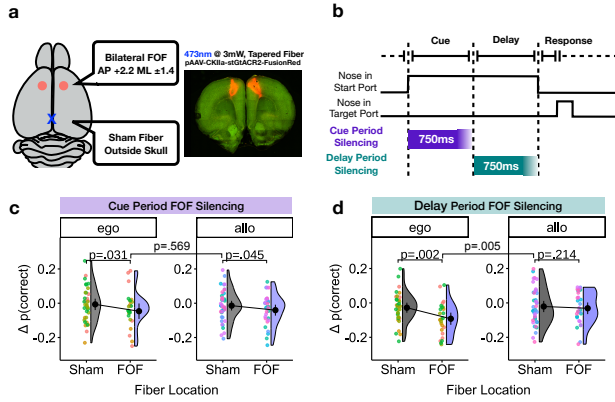


Figure 4. Comparision of optogenetically FOF silencing between two tasks **a.** Illustration for virus injection and fiber implantation location at bilateral FOF and a sham fiber implantation above the skull (Left). Coronal sections of a rat brain expressing stGtACR2-FusionRed (Right). **b.** Photoinhibition of bilateral FOF during the different task epochs. **c.** Effects of cue period photoinhibition on behavior in the Ego task (Left) and the Allo task (Right). Y axis: fraction of correct choices for laser on trials - laser off trials for each session (dots, colored by different animals). **d.** Effects of delay period photoinhibition on behavior in the Ego task and the Allo task. Same number of sessions and rats as c.

mechanism for the Ego task) so that the movement can be planned ahead of time to make the choice faster; therefore, we set the 'memory cost per bits' for FOF to 0.3 bit. Maintaining the memory in the auditory system or maintaining the upcoming spatial-location is less straightforward; therefore, we set the 'memory cost per bits' for those memories as 1 bit.

We defined a selective excitation module to select different memory systems based on the cost. The overall cost of each memory system C_m was defined as the 'memory cost per bits' \times 'number of bits to store'. For example, doing the Ego task with FOF will yield $0.3 \text{ (memory cost per bit)} \times 1 \text{ bit}$ (binary leftward/rightward choice, Supplementary Figure 1a, Left), doing the Ego task with memory in the auditory system will yield a higher cost for $1 \text{ (memory cost per bit)} \times 1 \text{ bit}$ (binary auditory cue). In the example of the Allo task, FOF will yield $0.3 \text{ (memory cost per bit)} \times 4 \text{ bits}$ (from 12 possible movement directions, Supplementary Figure 1a, Right); meanwhile, the auditory/spatial-location memory will only yield $1 \text{ (memory cost per bit)} \times 1 \text{ bit}$ (binary auditory cue/target location). The selective excitation module adjusted the weight for each system w_m by optimizing the overall cost, which is the square sum of the overall cost for each system \times the weight on that memory system: $\sum(w_m C_m)^2$.

Besides the selective excitation module, We modeled two potential network modules that directly support two different mechanisms of short-term-memory: 1) FOF network that maintains the planning of future movement egocentrically; 2) Sound cue network that maintains the auditory cue. The selective excitation module returns the weight for each of the network, based a dynamic optimization computed based on the cost we defined previously. (Figure 5a, see Methods).

After 100 trials iteration, the distribution of weight for FOF (w_{FOF}) selected to excite FOF for the Ego task but not the Allo task (Figure 5b). The FOF network was modeled as attractor network as previous work^{28,29}, with selective exciation, the activity of one attractor node showed selective activity for the ego task for upcoming left/right chocie (Figure 5c), but not for the allo task (Figure 5d). We were able to decode choice from FOF network during delay period, for the ego task but not the allo task (Figure 5e).

420 This replicated our findings from FOF recording in real animals during the delay period
 421 (Figure 3b). Moreover, silencing the FOF network during the delay period inhibited the
 422 selective activity for choice impaired task performance for the model in the ego task but
 423 not the allo task (Figure 5f).

424 Given excitation produced the ramping dynamics of the attractor network (Figure
 425 5b), we were able to decode the time in trial with a linear regression model from
 426 network activity in the Ego task (Figure 5h). We quantified the time decoding per-
 427 formance as R^2 between predicted time and actual time during the trial, the model
 428 predicted a higher decoding R^2 for the ego task than the allo task (Figure 5i). Decoding
 429 from real FOF recording confirmed this prediction: we observed overall better decoding
 430 for time for the ego task than the allo (Figure 5j,p<.001, permutation test), suggest-
 431 ing that FOF neuron populations received more excitation for the ego task. This matched
 432 with the recent work about ramping dynamics in M2⁴².

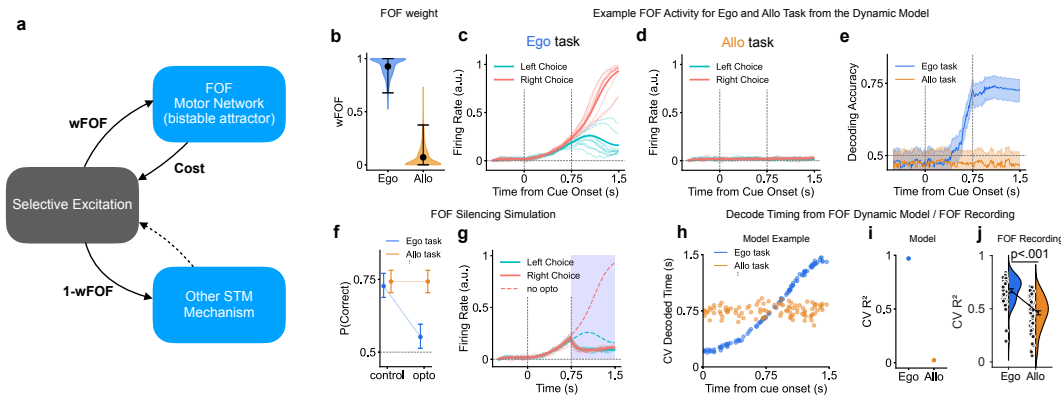


Figure 5. Mechanistic Model Supporting Flexible Working Memory Based on Task and Performance Cost **a.** Schematic of the model. The controller, a higher-order area, governs the use of different networks for working memory. **b.** Distribution of wFOF (weight of using FOF network) after 100 iterations from 1000 randomized trials. **c.** Example activity of one FOF network node in the Ego task, showing bifurcation during the delay period for future left/right choice. Light traces represent activity from other example trials with similar patterns. **d.** Example activity of one FOF network node in the Allo task, showing no selective activity for future choice. **e.** Time course decoding accuracy in the FOF network for left/right choice, colored differently for Allo and Ego tasks. Lines represent the mean, shaded areas are 95% confidence intervals (CI). **f.** Task performance with FOF network silencing (removing 90% FOF excitation) for both Ego and Allo tasks. Circles and error bars represent the mean and 95% CI, respectively. **g.** Example activity of one FOF node with FOF silencing in the Ego task during the delay period. Similar to C, solid traces show the mean activity for future left/right choices, while dashed lines represent the mean activity without silencing. Shaded areas indicate the silencing period (0.75s to 1.5s). **h.** Example decoding results for time during the trial. The Ego task shows a strong linear relationship between decoded time and actual time. **i.** Time decoding mean R^2 for the Allo and Ego tasks from FOF model activity. **j.** Time decoding R^2 for the Allo and Ego tasks from FOF recording data. Circles for individual recording sessions. Violins show kernel density estimation for R^2 across all sessions. Error bars: S.E.

433 **Flexible and rapid recruitment of FOF after task reduction support
 434 model prediction**

435 The excitation selection in our model was based on the cost of the task. Although for the
 436 allo task the excitation for FOF is weak, if the task was reduced to the simple version of

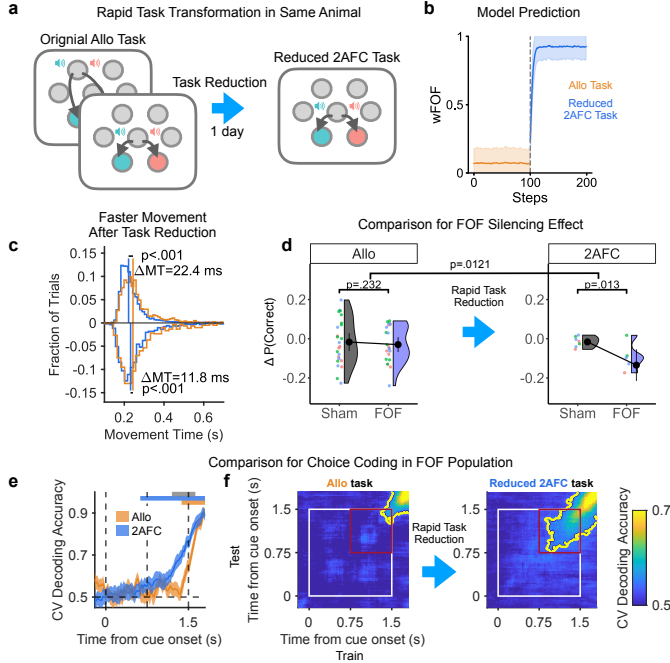


Figure 6. Rapid task transformation re-recruited FOF for the short-term memory for choice **a**. Schematic of the model. The controller, a higher-order area, governs the use of different networks for working memory. **b**. Development of wFOF after transitioning from the Allo task to the simpler 2AFC task. The solid line represents the mean wFOF (from 1000 randomized trials) over each iteration step. Shaded areas indicate the standard deviation (SD) of wFOF at each step. **c**. Movement time(MT) distribution for the original Allo task and the reduced 2AFC task, from center-port started trials. Histograms of MT from Allo (Orange) and reduced 2AFC (Blue) tasks are shown here for hits (Top) and error (Bottom) trials. Vertical line: median of RT. **d**. Effects of delay period photoinhibition on behavior in the original allo task (Left) and the reduced 2AFC task (Right). Y axis: fraction of correct choices for laser on trials - laser off trials for each session (dots, colored by different animals). **e**. Averaged decoding accuracy from 100 pseudo populations over the time course of the trial. Shaded indicate 99% C.I. The blue and orange thick bar at the top indicates the time when the decoding accuracy was significantly above chance for the allo and reduced 2AFC task, respectively ($p < .01$, permutation test with label shuffled null distribution, FDR correction). The grey bar at the top indicates the time when the decoding accuracy was significantly different on the allo verse reduced 2AFC task ($p < .01$, permutation test, FDR correction) **f**. Choice decoding accuracy with cross-window decoding. Colors of the heat maps indicate the decoding accuracy for choice, averaged across 100 pseudopopulations. The decoders were trained at one time window and tested at another. Contours, $p < 0.01$ (extreme pixel-based test). Pseudopopulations were constructed from neurons with at least ten trials for each of the left/right choice trials started from the center port. The white and red box highlighted the fixation and delay period, respectively.

437 the delay response task that always started from the center port (Figure 6a), the model
438 predicted that the selective activation would be pointed to FOF rapidly after the switch
439 (Figure 6b). That switch was mainly driven by the change of the cost. Before task
440 switch, there was 4 bits of memory cost to represent 12 potential movement direction
441 for the allo task. That cost was rapidly reduced to 1 bit after the task switch: MidC
442 started left/right choice trial was a binary choice.

443 We verified this prediction on real animals. For some of rats on optogenetics ($n=3$
444 rats) or FOF recording experiment ($n=4$ rats), we rapidly transferred them to the reduced
445 version of the task after several sessions of experiments (Figure 6a, see Figure 7a for
446 details). For MidC port start trials that chosen left/right bottom ports, the movement
447 time (MT) that defined as the time from exciting the MidC port until reaching the chosen
448 port was, on average, 22.3 ms faster after the rapid task reduction for correct trials
449 (Figure 6c from $n=7$ rats, Allo task: Median MT = 243.9ms (240.8ms to 247.5ms) 95%
450 CI, 1,226 trials; reduced 2AFC task: 221.6ms (219.9ms to 222.8ms) 95% CI, 4,554 trials,
451 $p<.001$, LRT). Yet the difference was smaller, the statistic power of this MT difference is
452 stronger than the faster MT we observed for allo task verse ego task (Figure 1e), because
453 this MT improvement was on the same rat (Supplementary Figure 7f), suggested that
454 after task reduction, the timing of sensory-to-motor transformation could be advanced.

455 We then compared the role of FOF before and after task reduction. Optogenetically,
456 we silenced FOF following the same experiment we performed in Figure 4. In
457 this analysis, we excluded 2 rats did not went through the task transformation part
458 of the experiment (yield $n=3$ rats). We performed the same analysis as in Figure 4
459 and described in the previous chapter. Instead of comparing the ego and allo tasks, we
460 compared the allo task and reduced 2AFC task after the rapid task transformation. For
461 delay period FOF silencing compared with Sham fiber laser delivery, we didn't observed
462 any significant laser modulation with $OPTO_{FOF}=0.0119$ in the allo task ($p=0.232$,
463 LRT, $n=24/22$ Sham/FOF sessions). However, after a rapid task transformation, we
464 observed a significant laser modulation for $OPTO_{FOF} = 0.1145$ ($p=0.013$, LRT, $n=7/6$
465 Sham/FOF sessions). We obtained a significant difference from the model comparison
466 that estimated the difference before and after task change ($p=0.0121$, LRT, Figure 6d).
467 Suggested that after a rapid task transformation, in 2-6 days, FOF became causally
468 contributed to the task.

469 We compared choice decoding performance before and after task reduction for MidC
470 start left/right bottom port choice trials to control for the same movement choice. We
471 performed the same pseudopopulation decoding as described in Figure 3b and the pre-
472 vious chapter. After rapid task transformation, the decoding accuracy for choice ramp
473 beyond significance earlier (Figure 6e, blue line), in the same group of rats (we excluded
474 one rat that didn't have signal unit signal here, $n=3$ rats, 10/19 sessions, 373/2,858 tri-
475 als from allo/reduced-AFC task). During the second half of the delay period, decoding
476 accuracy in the reduced 2AFC task was significantly higher than the original allo task
477 (Figure 6f, thick grey bar for $p<.01$, from permutation test). We also examined the
478 stability of representations by training decoders at one time and then testing them at
479 other times for pseudopopulations of allo and reduced 2AFC task. We found a significant
480 plateau is emerging after task transformation (Figure 6f, right panel). Our recording
481 results suggested that, after a rapid task transformation, FOF started to maintain a
482 stable coding for choice, this stable representation was causal for the upcoming choice.
483 Yet weaker than the stable coding in the ego task that we presented in the previous
484 chapter (Figure 3b,d), given the task transformation was happening within days, the
485 significantly earlier decoding of choice together with the significant FOF silencing effect

486 provided a solid evidence that the FOF was re-recruited for planning after the rapid task
487 reduction.

488 Discussion

489 Our study reveals that frontal-orienting-field (FOF, or M2) in rodents is crucial for
490 short-term memory of upcoming movements—but only when the task can be performed
491 in egocentric reference frame easily. When the same animals performed an allocentric
492 version of the task, M2 activity no longer encoded the upcoming (allocentric) choice
493 for planning purposes, nor was it causally necessary, unless the task was simplified to
494 a binary (2AFC) version that meet easy egocentric planning. These findings refine the
495 classical notion of rodent M2 as a universal buffer for delayed responses^{5,6,15,26,27} by
496 revealing M2’s context-dependent role: it strongly participates only when short-term
497 planning can be accomplished via a low-cost, egocentric code.

498 A key interpretation here is that M2 can encode both allocentric and egocentric
499 signals⁶, but it plans movements chiefly in body-centered coordinates. Allocentric sig-
500 nals within M2 appear more like “representations” (e.g., of start port location) rather
501 than sustained, prospective activity for guiding movement. This parallels evidence from
502 posterior parietal and retrosplenial cortices^{23,25,43,44} and hippocampal maps^{23,45}, which
503 handle world-centered transformations more natively. M2 thus functions as an ego-
504 centric planning hub, engaged when the motor plan itself can be cast in a left/right
505 or otherwise body-centric format, while deferring to other cortical networks for purely
506 allocentric tasks.

507 A second perspective concerns the distribution of short-term memory across cortical
508 areas. Earlier rodent work^{5,6,15,26,27} concluded that M2’s persistent delay activity sup-
509 ports memory of upcoming movements, suggesting a motor buffer. Our data refine this,
510 showing that M2’s delay-period involvement depends on task simplicity: if the required
511 memory can be compressed to a binary, self-centered choice, M2 steps in as a low-bit
512 buffer. If, however, the task calls for more elaborate or allocentric representations, other
513 regions (e.g., parietal, retrosplenial, entorhinal, or auditory cortex) appear to store the
514 relevant information. This interpretation aligns with the cost-benefit argument that
515 M2 is only recruited when it can effectively reduce the memory load to an egocentric
516 movement plan^{30,32,39,40,40,41,41}.

517 A particularly striking observation is the rapid reconfiguration of M2-based activi-
518 ty when we switched from a fully allocentric task back to a simpler 2AFC structure.
519 Within just a few sessions, M2 reacquired strong, persistent coding of movement di-
520 rection, paralleling its renewed causal impact on behavior. While prior work often
521 documents slower, learning-related neural changes^{46–48}, or a change of neural encod-
522 ing dynamics in one brain area⁴⁹, swift reversion to earlier planning regimes—based
523 solely on task simplification—has not been reported. To our knowledge, there is no
524 direct prior demonstration of M2 switching so quickly between “off” and “on” states
525 of delay period activity, solely based on whether the reference frame or memory load
526 is simplified. This suggests a high degree of plasticity or “meta-flexibility” in frontal
527 circuits, where the cost-benefit balance for storing an egocentric plan can be recalcul-
528 ated rapidly. This raises intriguing questions about the underlying plasticity or gating
529 signals, possibly top-down modulatory inputs from higher-order cognitive controlling
530 areas (i.e. mPFC⁵⁰, OFC⁵¹, PFC⁵²).

531 Looking ahead, several lines of inquiry can illuminate how the allocentric task is

532 maintained without M2 involvement—and why M2 can so rapidly reconfigure after task
533 simplification:

534 **1: Allocentric vs. Sensory-Based STM.** The brain may store auditory cues in
535 higher-order auditory or association cortex^{32,39}, deferring movement planning until just
536 before execution. Alternatively, the allocentric plan itself (i.e., “where” to move in world-
537 centered coordinates) could reside in posterior parietal or retrosplenial circuits^{23,25,43}.

538 **2: Transformation into Egocentric Coordinates.** Regardless of whether the animal
539 maintains a sensory trace or an allocentric motor goal, the final movement is
540 inevitably body-centered. This transformation step likely adds “action cost,” explaining
541 why M2’s simple left/right plan remains the default for easy tasks. Investigating how
542 the brain executes this last-mile transformation—perhaps via multi-area recordings⁵³
543 —would reveal the precise interplay among parietal, frontal, and subcortical nodes.

544 **3: Rapid Task Transformation Mechanisms.** Equally important is understanding
545 the neural processes that enable M2 to “snap back” into an egocentric memory role after
546 the task is stripped down to 2AFC. Future experiments would involve identifying and
547 simultaneously recording from the brain region(s) responsible for sustaining allocentric
548 task demands, in parallel with M2, using high-density silicon probes^{53,54}. By tracking
549 both sites in animals switching between allocentric and simplified 2AFC conditions, one
550 could directly observe a redistribution of short-term memory signals from the “allocen-
551 tric region” back to M2 when task complexity decreases. In addition, recording from
552 higher-order frontal areas such as the medial prefrontal cortex (mPFC) might reveal sub-
553 populations of neurons specifically involved in governing the transition between these
554 distinct STM strategies. Finally, to test the causal role of such putative “switching”
555 neurons, one could transiently perturb M2 and/or mPFC (e.g., optogenetic or chemo-
556 genetic inactivation) during task transitions, asking whether these interventions impede
557 or alter the normal reconfiguration of STM representations. Such experiments would
558 decisively link circuit-level reorganizations of memory states to higher-order executive
559 control processes.

560 Overall, our results establish that M2 is not a universal short-term memory store
561 but a specialized, egocentric planning module. It robustly encodes a low-bit “move
562 left/move right” plan when that strategy is feasible and beneficial, yet allocentric or
563 more elaborate memories appear to be handled by other cortical and subcortical cir-
564 cuits. By demonstrating M2’s disappearance from the memory loop in fully allocentric
565 tasks, followed by its rapid re-engagement when the task is simplified, we highlight the
566 impressive contextual flexibility of frontal circuits. Such findings encourage broader
567 multi-area investigations into how neural systems dynamically weigh and select among
568 memory strategies—egocentric, allocentric, or purely sensory-based—in real time, shed-
569 ding light on the fundamental question of how cost-benefit forces shape short-term
570 memory allocation in the mammalian brain.

571 Acknowledgements

572 We thank Lillianne Teachen, Yingkun Li, Aline Rampini, Nengneng Gao, Santhia Ra-
573 jagobalan, Mingming Chen and Nicolas Chapelot for training animals and technical

574 assistance. We thank Rob Campbell and SWC Advanced Microscopy Facility for the
575 infrastructure for brain imaging.

576 Contributions

577 J.L. and J.C.E. designed the behavioral task and conceptualized the study. J.L. de-
578 signed and built the hardware for high-thoughput behavioral training, optogenetics
579 and electrophysiology recording. J.L. implemented and programmed the task and train-
580 ing pipeline. A.X and J.L. trained the SLEAP model for video analysis and J.L. analyzed
581 and quantified the video data. J.L. analyzed the behavioral data. J.L. and C.B. per-
582 formed the surgeries with the nursing help from A.X. and L.L. J.L., A.X., C.B., L.L.
583 collected the electrophysiology and optogenetics data. J.L. analyzed the data from elec-
584 trophysiology and optogenetics experiment. A.A. and J.L. implemented the modeling
585 part under the supervision from J.C.E. and C.C. The paper was written by J.L. and
586 J.C.E. with comments from the other authors. C.C. supervised the modeling part of
587 the work and J.C.E. supervised all aspects of the work.

588 Methodology

589 Subjects

590 A total of 3 male Sprague Dawley rats (Vital River, Beijing, China) and 21 male and
591 female Lister Hooded rats (#603, Charles River, London, UK) were used for this study.
592 Animals were paired housed during the training period and then single housed after
593 electrode or fiber implantation. Of these 24 animals, 9 Lister Hooded rats were used
594 for FOF optogenetics experiment, another 15 rats were used for *in vivo* electrophysi-
595 ology recording experiment in FOF. Animals were water restricted in their home cage
596 in order to control water intake but the body weight was closely monitored daily to
597 ensure their health. All rats were kept on a reversed 12 hour light-dark cycle and were
598 trained during their dark cycle. Animal use procedures (for 3 male Sprague Dawley rats)
599 were approved by New York University Shanghai International Animal Care and Use
600 Committee following both US and Chinese regulations. Animal use procedures (for 21
601 male Lister Hooded rats) were approved by Home Office of the United Kindom (Project
602 License: PE4FA53CB).

603 Behavioral apparatus

604 Animal training took place in custom behavioral chambers inside sound- and light-
605 attenuating boxes. Each chamber ($23 \times 23 \times 23$ cm for training rigs and 23×23
606 $\times 45$ cm for recording rigs) was fit with 8 nose ports arranged in four rows (figure
607 1a), with stero speakers located on the left and right side. Each nose port contained
608 a pair of blue and a pair of yellow light emitting diodes (LED) for delivering visual
609 cue, as well as two infrared LED/phototransistor pairs for detecting rats' interactions
610 with the port. The port in the bottom row contained a stainless steel tube and a
611 solenoid valve for dispensing precisely measured liquid rewards. The LEDs, speakers,
612 water valves and the IR pairs is controlled by Bpod (https://github.com/sanworks/Bpod_Gen2), with some modification design: (1)more I/O to control more LEDs; (2)use a
614 special designed hysteresis comparator array to digitalize the IR output to avoid jittering;
615 (3)better ground/isolation layout to prevent gound loop. Specifically, we intergrated all

616 of the LEDs and IR pairs into a single PCB (the pokewall, as in figure 1A) which
617 was connected to the bpod main hardware with a single ribbon cable and another 5V
618 USB supply. Those design greatly improved the stability and reliability of the whole
619 behavioral system. For the detailed design please refer to our open-sources repository
620 (<https://gitlab.com/sainsbury-wellcome-centre/delab/bpod-auto>).

621 Behavioral Task and Training Pipeline

622 We developed two task variations based on the classical delayed discrimination task for
623 two groups of water-deprived rats. Both task variations followed the same timeline.
624 At the beginning of each trial, one of the operant ports was randomly illuminated as
625 the "start port." Rats were required to fixate in the start port for 1.5 s until a go cue,
626 constituting the "fixation period." During the first 0.75 s, a binary auditory cue was
627 presented (30 Hz or 68 Hz clicks, with each click lasting 0.003 s at a frequency of 8000
628 Hz, calibrated to 78 dB peak amplitude using the **make_clicks** function in erlichlab
629 utilities⁵⁵). This was followed by a 0.75 s delay period.

630 After the fixation period, rats withdrew from the start port and moved to a target
631 port. A correct target port selection resulted in water reward availability at the re-
632 ward delivery port. Incorrect choices triggered an error sound, and a new trial became
633 available after a short inter-trial interval (2–10 s; Figure 1a). Early withdrawal from
634 the start port before fixation completion led to a "soft violation," requiring the animal
635 to repeat the trial. Early withdrawal trials were excluded from analyses except when
636 calculating early withdrawal rates (Supplementary Figure 6).

637 The definition of the target port depended on the task context and start port:

- 638 • **Egocentric (Ego) Task:** The correct target port was the left or right port
639 adjacent to the start port, determined by the sound cue (blue/red for 30 Hz/68
640 Hz clicks, respectively; Figure 1c, left). As the correct target port shifted with the
641 start port on each trial, this task required egocentric spatial coding, resulting in
642 eight trial types spanning two movement directions.
- 643 • **Allocentric (Allo) Task:** The correct target port was fixed in physical space,
644 with the bottom-left/bottom-right port corresponding to the blue/red sound cues,
645 respectively (Figure 1c, right). This allocentric spatial coding yielded 12 trial
646 types and 10 unique movement directions.

647 Training Pipeline

648 Rats underwent a structured training pipeline to acquire the final task. Training com-
649 prised three phases:

650 1. **Operant Conditioning Phase:** In this phase, rats became familiar with the
651 training apparatus and learned to associate illuminated ports with water rewards.
652 Training progressed through distinct stages:

- 653 • **Stage 1:** The reward port was illuminated, and rats received water upon
654 entry. Advancement to the next stage required six consecutive correct trials.
- 655 • **Stage 2:** All operant ports were illuminated, and poking in any lit port
656 activated the reward port. The number of illuminated ports was gradually
657 reduced from eight to one. Progression required six consecutive successful

658 trials without errors (e.g., pokes in unlit ports) or timeouts (no poke within
659 60 s of trial initiation).

660 2. **Auditory Cue and Task Rule Phase:** In this phase, rats learned the asso-
661 ciation between auditory cues and target ports. Fixation was not required; rats
662 could initiate a trial by poking the start port, after which the auditory cue was
663 played until choice. Initial training used blocked trial types, with block switching
664 probabilities increasing after each correct trial (starting at 0.02).

665 3. **Fixation and Timing Phase:** This phase introduced fixation and timing re-
666 quirements. Initial fixation times were set to 1100 ms and gradually increased by
667 20 ms increments based on performance until reaching 1500 ms. Once fixation
668 timing was stable, auditory cue durations were reduced from 1100 ms to 750 ms
669 using the same incremental approach.

670 Rats were trained daily for 80 minutes. The complete training process typically
671 required 2–4 months.

672 **Surgery**

673 The rats were anesthetized with isoflurane and placed in a stereotaxic apparatus (David
674 Kopf Instruments). The scalp was shaved, washed with ethanol and iodopovidone and
675 incised. Then, the skull was cleaned of tissue and blood. The stereotax was used to
676 mark the locations of craniotomies for the FOF (+2.5 AP, ± 1.4 ML mm from Bregma),
677 relative to Bregma on the skull. Then a 1.5mm craniotomy was drilled, followed by an
678 entire dura resection. The craniotomy was then filled with saline saturated Gelfoam to
679 protect the brain tissue while the skull was coated with a thin layer of C&B Metabond
680 (Parkell, Inc; New York) and a 1-3mm high moat built around the craniotomy using the
681 Absolute Dentin (Parkell, Inc; New York).

682 For electrophysiology surgery, silicon probes (Cambridge NeuroTech/Neuropixel 1.0)
683 were implanted in either left or right FOF. The silicon probes were adhered to nano-
684 drives (Cambridge NeuroTech, or R2Drive⁵⁶) with super-glue before implant. Ground
685 wires were soldered to titanium ground screws located above primary visual cortex. The
686 silicon probe was slowly lower into the brain until all the recording sites were immersed
687 into the tissue (1.3mm DV for the H3 probes, and 0.5mm DV for the E probes and F
688 probes, 3.6mm for Neuropixel 1.0 probes with 10 degree for ML).

689 For optogenetics surgery, we slowly injected 400uL AAV virus solution (pAAV-
690 CKIIa-stGtACR2-FusionRed, AddGene #105669, about 5×10^{12}) using nanoinjector
691 into FOF bilateraly. Tapered fibers (MFC_200/245-0.37_4.5mm_ZF2.5(G)_TP1.5,
692 Doric Lenses Inc.) were inserted 1.2 mm into the cortex measured from the brain surface
693 for each craniotomy for bilateral FOF.

694 The craniotomy was filled with Dura-Gel (Cambridge NeuroTech), and then silicon
695 probes or the optic fiber was cemented to the skull with Absolute Dentin. Vetbond (3M,
696 U.S.) was applied to glue the surrounding tissue to Absolute Dentin. The animals were
697 given 5 days to recover on free water before resuming training.

698 **Electrophysiology Recording and Spike Sorting**

699 For Cambridge Neurotech probe, Neural activity was digitized at 30 kHz, amplified and
700 bandpass filtered at 0.6-7500Hz using a 64 channel intan headstage (RHD2164, Intan

701 Technologies, https://intantech.com/files/Intan_RHD2164_datasheet.pdf), the SPI
702 cable of the intan headstage was tethered to a commutator to allow free spinning
703 (Shenzhen Moflon Technology, MMC250), and all the raw data was processed using
704 the Open Ephys acquisition board (<https://open-ephys.org/acquisition-system/eux9baf6a5s8tid06hk1mw5aafjdz1>) connected to a computer to visualize and store
705 the neural signals. The probes were turned down $\sim 100\mu\text{m}$ every day for 4-6 days until
706 the white matter was reached. For Neuropixel 1.0 probe, we used acquisition hard-
707 ware from NI (a PXIe-1071 Chassis) with a Neuropixel recording module (PXIE_1000,
708 IMEC). Data was monitored and recorded with SpikeGLX software (<https://github.com/billkarsh/SpikeGLX>).
710

711 During the recording, a serial TTL messages encoding the current trial number was
712 sent from our behavioral control hardware to the acquisition system to synchronize the
713 neural signal with the behavior data ([https://gitlab.com/sainsbury-wellcome-centre/delab/bpod-auto/-/wikis/interaction-with-other-system-\(Syncing-and-Triggering\)](https://gitlab.com/sainsbury-wellcome-centre/delab/bpod-auto/-/wikis/interaction-with-other-system-(Syncing-and-Triggering))).
714

715 Offline spike sorting was performed by using **Kilosort v2**⁵⁷ for Cambridge neu-
716 rotech probe recording or **kilosort v4**⁵⁸ for neuropixel probe recording with the de-
717 fault settings. Spike clusters were manually curated using Phy <https://github.com/cortex-lab/phy>. The quality metrics and waveform metrics for sorted units were com-
718 puted using package: **ecephys spike sorting**(https://github.com/AllenInstitute/ecephys_spike_sorting)⁵⁹. Specifically, we selected units with averaged firing rate
719 $>1\text{Hz}$, signal-to-noise ratio >1.5 , and a presence ratio >0.95 over the course of record-
720 ing sessions.
722

723 Optogenetics Experiment

724 The implanted fiber was connected to one (for unilateral silencing or light delivary for the
725 control fiber) or two (for bilateral silencing) 0.6 m optic fiber cable (OPT/PC-FC-FCF-
726 200/230-HD-0.6L-MC KIT, Plexon Inc.). The other end of fiber cable was connected to
727 a dual fiber rotary joint (FRJ_1x2i_FC-2FC_0.50, Doric Lenses Inc.) mounted in the
728 ceiling of the sound attenuation chamber. This was connected to a 473 nm laser (473nm
729 LX 50mW LASER SYSTEM, OBIS Inc.) with a variable optic attenuator (VOAMMF,
730 Thorlabs Inc.) and an optic patch cable (M123L01, Thorlabs Inc.). Laser was analog
731 modulated by Pulse Pal (1102, Sanworks LLC) which triggered by Bpod with 5V TTL.
732 The laser power was calibrated by a laser power meter (PM20A, Thorlabs Inc.) before
733 and after every session to be 3mW at fiber end.

734 Videography

735 We used USB web camera (FIT9730, DFROBOT) to record video from top-down view
736 during behavior session. Video were acquired at 640×480 pixels and 20 frames per
737 second. Mice performed the task in complete darkness, and videos were recorded under
738 infrared 940 nm LED illumination. We developed a custom software controlled the video
739 acquisition for each session (<https://gitlab.com/sainsbury-wellcome-centre/delab/devops/zmq-video-server>).
740

741 Histology

742 We imaged the brains using serial section⁶⁰ two-photon⁶¹ microscopy. Our micro-
743 scope was controlled by ScanImage Basic (MBF Bioscience) using BakingTray, a cus-
744 tom software wrapper for setting up the imaging parameters(<https://github.com/>

745 SWC-Advanced-Microscopy/BakingTray). Images were assembled using StitchIt(<https://github.com/SWC-Advanced-Microscopy/StitchIt>).
746

747 **Behavioral data analysis**

748 We excluded all timeout trials (no choice made within 2 s) and fixation violation trials
749 (failure to maintain fixation for 1.5 s in the start port). Additionally, to account for
750 forelimb interference with the IR beam during movement initiation, we excluded trials
751 where port entry was detected within 0.2 s after the go cue (3.71% of trials removed).
752 The hit rate was calculated as the fraction of trials in which the animal reached the
753 choice port, relative to all remaining trials after these exclusions. This result was shown
754 in Figure 1d. Movement time (MT) was defined as the interval between withdrawal
755 from the start port (following the go cue) and entry into the choice port, calculated
756 using trials initiated from the MidC port after applying the aforementioned exclusions.
757 This distribution of MT was shown in Figure 1e and Supplementary Figure 1c. To
758 compare the difference of MT between the different tasks, we employed a mixed-effects
759 model (using lme4 (version 1.1-29) R package) that considered task type as predictors
760 of $\log_{10}(MT)$. The variability for each subject was modeled as a random effect.

761 In GLMM formula syntax:

$$\log(MT) \sim 1 + task + (1|subjid) \quad (1)$$

762 where *task* is for the allo/ego task or allo/reduced-2AFC task as a factor. *subjid*
763 is the rat ID as factor to compensate for subject-by-subject variability. This model was
764 fitted separately for correct or in-task error trials. We regarded this model as the full
765 model *mf* (Equation 1). To statistically quantify the difference of MT distribution
766 between allo/ego task or allo/reduced-2AFC task, we drop the interaction *task* term
767 from the fixed effects and fit a reduced model *mr* (Equation 2) as follows:

$$\log(MT) \sim 1 + (1|subjid) \quad (2)$$

768 The likelihood ratio test was performed using *lrtest(mf, mr)* (from the lmtest R
769 package) to determine whether the MT in different tasks can be different statistically.

770 **Video data analysis**

771 We used SLEAP³⁵ to track manually defined body key points (nose, left ear, right ear,
772 neck, Figure 1f) from video frames recorded for each session. Separate models were used
773 to track animals that have different implant type (optic fiber, or recording probe). We
774 manually labeled about 3000 frames for each model to generate the dataset to train
775 each tracking model from randomly picked frames from different sessions. Training was
776 performed using the default setting parameters of SLEAP. Then the trained model was
777 used to predict the position of each key point for all frames of all sessions. We then
778 calculated vector angles between the pair of each point using the x,y coordinate of each
779 points.

780 For each trial, the vector data (3-dims, left-ear/right-ear/neck to nose angle, Fig-
781 ure 1f) was aligned to the trial onset (using **cdraster** function in erlichlab utilities⁵⁵,
782 Figure 1g), or choice port (target) arrival. At each timepoint for each individual rat,
783 we used logistic regression with LASSO regularization and 10-folds cross-validation that
784 took the vector angles as input to predict the animals' choice (using **fitclinear** function

785 in MATLAB). We concatenate all data from all sessions for each individual rats. Only
 786 MidC port started trials that animals hit the correct target or the opposite target were
 787 included for the video posture analysis to control for the same up-coming movement.
 788 We averaged the choice decoding accuracy of all rats at each timepoint for each task,
 789 weighted by the number of trials. This result was shown in Figure 1h and Supplementary
 790 Figure 1d.

791 Electrophysiology Data Analysis

792 **Single-Neuron Analyses** Spike times were aligned to the sound cue onset within a
 793 2.5 s time window (-0.5 s before cue onset to 0.5 s after fixation end) for the raster and
 794 peri-stimulus time histogram (PSTH) plots. The bin size was set to a resolution of 10 ms
 795 and smoothed with a causal half-Gaussian kernel with a standard deviation of 200 ms.

796 To evaluate whether the firing of each cell could predict upcoming choice during
 797 the delay period ($0.75 - 1.5\text{ s}$ after cue onset), spike counts were calculated for each
 798 trial during this period. A label-shuffling permutation test (5000 iterations) was used
 799 to estimate the p -value for choice tuning, and cells with $p < 0.05$ were identified as
 800 choice-selective.

801 To quantify choice tuning of each cell, a selectivity index for choice tuning was defined
 802 as:

$$\text{Choice Selectivity Index} = \frac{\overline{nSpk}_{\text{choice_ipsi}} - \overline{nSpk}_{\text{choice_contra}}}{\overline{nSpk}_{\text{choice_ipsi}} + \overline{nSpk}_{\text{choice_contra}}}$$

803 where $\overline{nSpk}_{\text{choice_ipsi}}$ and $\overline{nSpk}_{\text{choice_contra}}$ are the average spike counts for ipsilateral
 804 and contralateral (with the recording hemisphere) choice trials during the delay period,
 805 respectively. Left/right was defined by target direction for the ego task or target port
 806 for the allo task. Only correct trials (correct choice port/direction entry corresponding
 807 to the cue) were included for the choice selectivity analysis.

808 To assess choice selectivity over the trial's time course, we applied a linear regression
 809 model at each time point using the MATLAB `fitglme` function with the formula:

```
810         firing_rate ~ 1 + choice_index
```

811 `Firing_rate` was estimated with a 250 ms sliding window (25 ms step size) from spike
 812 times aligned to cue onset. `Choice_index` was a binary variable (0 or 1) corresponding
 813 to left or right choice based on the cue. A $p < 0.05$ threshold for the `choice_index`
 814 coefficient was used to identify choice-selective cells at each time point. The percentage
 815 of such choice-selective cells was then calculated across time points. Both correct and
 816 opposite-choice trials (animals chose the opposite choice port/direction based on the
 817 definition of the cue, we defined as in-task error trials) were included for choice selectivity
 818 over time analysis.

819 A mixed-effects linear regression model was implemented to evaluate the contribution
 820 of start port position to firing rates in the FOF cells, independent of choice. Using the
 821 MATLAB `fitglme` function, the formula was:

```
822         spike_counts ~ 1 + start_port_index + (1|choice_index)
```

823 Here, `spike_counts` represented the number of spikes per trial during the delay pe-
 824 riod, and `start_port_index` (1–5) denoted the X-axis location of the five start ports.
 825 `Choice_index` was a binary variable (0 or 1) for left or right choice, included as a ran-
 826 dom effect to control for potential confounding effects of choice on start-port activity. A

827 $p < 0.05$ threshold for the `start_port_index` coefficient identified start-port-selective
828 cells.

829 To assess start-port selectivity over the trial's time course, the same mixed-effects
830 regression model was applied to `firing_rate` (estimated with 250 ms window, 25 ms step
831 size) aligned to cue onset. Cells with $p < 0.05$ for `start_port_index` were identified as
832 start-port selective, and the percentage of such cells was calculated over time points.

833 Start-port tuning for each neuron was quantified using a selectivity index defined as:

$$\text{Start-Port Selectivity Index} = \frac{\overline{n\text{Spk}}_{\text{ipsi}} - \overline{n\text{Spk}}_{\text{contra}}}{\overline{n\text{Spk}}_{\text{ipsi}} + \overline{n\text{Spk}}_{\text{contra}}}$$

834 where $\overline{n\text{Spk}}_{\text{ipsi}}$ and $\overline{n\text{Spk}}_{\text{contra}}$ are the average spike counts for ipsi-lateral and contra-
835 lateral (with the recording hemisphere) choice trials starting from the leftmost and
836 rightmost ports, respectively, during the delay period. These counts were estimated
837 using the mixed-effects model mentioned above, with start port and choice as inputs.

838 **Pseudopopulation Decoding** For decoding, the firing rate of each cell was estimated
839 using a 250 ms sliding window with a 25 ms step size, aligned to cue onset. To compare
840 choice decoding performance, we generated 100 pseudosessions for each task. For each
841 pseudosession, we randomly sampled 100 cells without replacement. For each selected
842 cell, we extracted 10 left-choice and 10 right-choice trials (from correct trials and in-
843 task error trials) that started from the MidC port to control for consistent planned
844 movement. This process yielded a 100 (cells) \times 20 (trials) $\times n_{\text{timebin}}$ matrix, D_{original} ,
845 for each pseudosession.

846 Principal component analysis (PCA) was then applied to D_{original} , with distinct
847 approaches depending on the analysis type: decoding comparison (Figure 3b, Figure 6e)
848 or cross-time decoding (Figure 3d, Figure 6f). For decoding comparison, PCA was
849 performed independently for each timepoint, and the top five principal components were
850 used. This resulted in a matrix $D_{\text{independent}}$ of dimensions 5 (PCA dims) \times 20 (trials) \times
851 n_{timebin} for decoding analysis. For cross-time decoding, the resampled data D_{original} was
852 concatenated along trials, creating a 2D matrix of dimensions 100 (cells) $\times (n_{\text{timebin}} \times$
853 20 trials), denoted as $D_{\text{concatenated}}$. PCA was applied to $D_{\text{concatenated}}$, we used top
854 five principal components and reversing the trial concatenation, a matrix D_{shared} with
855 dimensions 5 (PCA dims) \times 20 (trials) $\times n_{\text{timebin}}$ was generated for decoding analysis.
856 Decoding was performed using multivariate linear classification models (`fitclinear` in
857 MATLAB) with leave-one-out cross-validation.

858 For decoding comparison plots (Figure 3b, Figure 6e), we analyzed each timepoint
859 dimension of $D_{\text{independent}}$ for each pseudosession, which was a 5 (PCA dims) \times 20 (trials)
860 matrix, to predict the label vector L (1×20 trials). To calculate the p -value for choice
861 coding at each timepoint, we shuffled the label vector L 5,000 times per pseudosession
862 to generate a null distribution of average decoding accuracy. A p -value for the compar-
863 ison between tasks was obtained using a permutation test with 10,000 shuffles of the
864 task label. To identify significant time windows for choice decoding in each task and
865 differences between tasks, we set the p -value threshold to 0.05 with Bonferroni correc-
866 tion. Significant windows lasting fewer than 9 consecutive timepoints were excluded to
867 remove unstable dynamics.

868 For cross-time decoding analysis (Figure 3d, Figure 6f), we trained a classifier for each
869 pseudosession at every $n_{\text{timepoint}}$ of D_{shared} (a 5 (PCA dims) \times 20 (trials) matrix) using
870 the label vector L . The classifier predicted the labels across all timepoints of D_{shared} with

871 leave-one-out cross-validation, yielding an $n_{\text{timepoint}} \times n_{\text{timepoint}}$ generalization matrix of
872 decoding accuracy that captured the temporal dynamics of choice coding⁶². To assess
873 statistical significance, we generated 1,000 null matrices by shuffling the label vector
874 L for each pseudosession. An extreme pixel-based permutation test⁶³ was applied to
875 compute p -values for each matrix element. Small significant "islands" smaller than $5 \times$
876 5 timepoints were excluded to remove unstable dynamics.

877 To compare start port position decoding, we generated 100 pseudosessions for each
878 task with the same way as we described for choice decoding, except that we sampled 10
879 left and 10 right choice trials (from correct trials and in-task error trials) for each of the
880 TopL,TopR,MidC start port without replacement, yeild 60 trials for each pseudosessions.
881 This process yielded a 100 (cells) \times 60 (trials) $\times n_{\text{timebin}}$ matrix, D_{original} , for each
882 pseudosession. For each trial, we used position index at X-axis of each port (-1 for TopL
883 port, 0 for MidC port and 1 for TopR port) to have a vector for start port position
884 of each trial as y (1×60 trials). D_{original} was concatenated along trials, creating a
885 2D matrix of dimensions 100 (cells) $\times (n_{\text{timebin}} \times 60 \text{ trials})$, denoted as $D_{\text{concatenated}}$.
886 PCA was applied to $D_{\text{concatenated}}$, and after projecting onto the top five components
887 and reversing the trial concatenation, a matrix D_{shared} with dimensions 5 (PCA dims)
888 \times 60 (trials) $\times n_{\text{timebin}}$ was generated for start position decoding analysis. Decoding was
889 performed using multivariate linear regression models (`fitrlinear` in MATLAB) with
890 10-folds cross-validation. We trained a decoder for each pseudosession at every $n_{\text{timepoint}}$
891 of D_{shared} (a 5 (PCA dims) \times 60 (trials) matrix) to predict the start position index y as
892 \hat{y} . The decoding performance was quantified as the R^2 between y and \hat{y} . The decoder
893 predicted the start position index of each trial as across all timepoints of D_{shared} , yielding
894 an $n_{\text{timepoint}} \times n_{\text{timepoint}}$ generalization matrix of decoding R^2 that captured the temporal
895 dynamics of start position coding⁶². To assess statistical significance, we generated
896 1,000 null matrices by shuffling the start position index y for each pseudosession. An
897 extreme pixel-based permutation test⁶³ was applied to compute p -values for each matrix
898 element. Small significant "islands" smaller than 5×5 timepoints were excluded to
899 remove unstable dynamics. To gernerate a direct statistical comparision of start position
900 decoding between task over time, we used the decoding R^2 that was from the same train
901 and test timepoint. The p -value for the comparison between tasks was obtained using a
902 permutation test with 10,000 shuffles of the task label, we set the p -value threshold to
903 0.05 with Bonferroni correction. Significant windows lasting fewer than 9 consecutive
904 timepoints were excluded to remove unstable dynamics.

905 **Single Trial Decoding** To decode choice for every trial in each session, we only
906 included trials started from MidC port that animals made choice for BotL/BotR ports
907 based on the task rule(both correct trials and in-task error trials), this yeild a $N \times T$
908 $\times n_{\text{timebin}}$ data matrix D_{sess} for each session, where N is the number of neurons in the
909 session, and T is the number of included trials. We also had a corresponding length
910 T vector for each session: L , which was 1 for chose-right trials and 0 for chose-left
911 trials. PCA was performed independently at each timepoint, and the top five principal
912 components were used. This resulted in a matrix Z_{sess} of dimensions 5 (PCA dims)
913 $\times N \times n_{\text{timebin}}$ for decoding analysis. Then we performed decoding at each timepoint
914 seperately using multivariate linear classification models (`fitclinear` in MATLAB)
915 with leave-one-out cross-validation. This yeild a $1 \times n_{\text{timebin}}$ decoding accuracy vector.
916 Performing this for all sessions finally yeild $N_{\text{session}} \times n_{\text{timebin}}$ decoding accuracy matrix.
917 To compute the latency of the rise in choice decoding performance between allo and

918 ego task, for each session we evaluated the time that the decoding accuracy of choice
919 reach a fixed threshold at %70, based on a previously reported method^{64,65}. Latency
920 comparision plot was generated by DataViz tool ([https://github.com/povilaskarvelis/
921 DataViz](https://github.com/povilaskarvelis/DataViz)).

922 To decode pending time in trial during the fixation period (for example, 0.1/0.2/0.3s
923 after cue onset). We includded all trials that animals made the choice based on the task
924 rule. We estiamted the firing rate with a 400 ms sliding window (100 ms step size) from
925 spike times aligned to cue onset, this yeild a $N \times T_{joint}$ matrix D_{time} for each session,
926 where N is the number of neurons and T_{joint} is the number of sample for time decoding,
927 which jointed the number of trials and number of timebins (for 1.5s fixation period with
928 100ms step size yeild 16 timebins) during the fixation period. PCA was then performed
929 on D_{time} , we used top 5 principal components yeild Z_{time} which is $5 \times T_{joint}$. We also
930 had a corresponding time label vector t for each session, which had the time relative
931 to the trial onset for each item. Then, we used multivariate linear regression models
932 (`fitrlinear` in MATLAB) to predict t with 10 folds cross-validation, yeild \hat{t} . We then
933 calcualted a R^2 between t and \hat{t} for each session to quantify time decoding performance.

934 **Coding Direction analysis** We visualized the dynamic of choice coding in population
935 coding space using coding direction analysis⁶. We estimated an $n \times 1$ vector, in the n
936 dimensional activity space that separated the response vectors in left/right chocie trials
937 from MidC started trials in both allo and ego task (from correct trials and in-task error
938 trials). Firing rate was estimated with a 400 ms sliding window (10 ms step size) from
939 spike times aligned to cue onset. For each left and right choice trials started from MidC
940 port, we computed the average firing rate \bar{x}_L and \bar{x}_R : an $n \times 1$ response vectors that
941 described the population response at each time point. We then calculated the difference
942 vector: $w_t = \bar{x}_L - \bar{x}_R$. We averaged the w_t values from mid-late fixation period (0.5s-1.5s
943 after cue onset) to obtain the coding direction of MidC started trials(CD_{MidC}).

944 For each trial, firing rate $x(n \times 1)$ at each time point were projected along CD : as
945 $CD^T x$. We then offset the trajectories for each session by subtracting the mean $CD^T x$
946 across all trials and time points in that session. We averaged those trajectories of each
947 session to generate the final activity visualization for choice.

948 We projected the CD_{MidC} to different trialtypes to test whether we have the same
949 coding space for the same choice across different start positions. For MidC started trials
950 that we estimated the CD_{MidC} , we performed 10-folds cross-validation that we always
951 generated the CD_{MidC} and projected the activity trajectories for different groups of
952 trials. For trials started from other ports, we estimated the CD_{MidC} using all of the
953 MidC-port-started trials for out-of-sample projections.

954 **Decoding Genrlisation Analysis** To statistically quantify the generalizability of
955 choice coding mechanism across different trialtypes that share similar movement/choice_port
956 in different task, we trained a multivariate linear classification model (`fitclinear` in
957 MATLAB) for MidC started trials for each session to predict Left/right choice label
958 vector L from spike counts matrix D_{raw} during the delay period. Here D_{raw} is a $N \times T$
959 matrix for N cells and T trials in that session, L is the choice label vector which was 0
960 for left choice and 1 for right choice.

961 We firstly predicted the choice label vector \hat{L} for all MidC started trials with 10-folds
962 cross-validation and quantified the decoding accuracy for each session. For each session,
963 we also predicted the choice label vector \hat{L} for other trialtypes started from other ports,

964 using the classification model trained with all MidC-started trials of that session as an
965 out-of-sample prediction accuracy.

966 Behavioral data analysis for optogenetics experiment

967 For optogenetic analyses, control trials were the no-laser trials from the same sessions
968 as a corresponding laser trial. Sham(control) sessions where the sessions that optic fiber
969 was plused into a control fiber which didn't entered the brain. Data analysis was not
970 performed blinded to the conditions of the experiments. No statistical methods were
971 used to pre-determine sample sizes, but our sample sizes are similar to those reported
972 in previous publications^{26,66}.

973 GLMMs were fit using the lme4 (version 1.1-29) R package and plotted using gg-
974 plot. To test whether bilateral FOF sailencing at different task epoch had any effect on
975 performance, we specified a mixed-effects model where $p(correct)$ (or μ , as a parameter
976 from binomial distribution) was a logistic function of laser on/off , fiber location (bilat-
977 eral FOF or sham) and their interaction as fixed effects. Session level variability were
978 modeled as random effect in this GLM.

979 To compare the difference of performance modulation from FOF sailencing between
980 allocentric and egocentric task, we employed another mixed-effects model that con-
981 sidered task type, laser status, fiber location, and their interactions as predictors of
982 $p(correct)$. The variability for each sessions(nested into each subjects) were modeled as
983 random effect.

984 In GLMM formula syntax:

985 For the optogenetic sailencing effect check per task condition,

$$\mu \sim 0 + isopto + FOF_fiber + isopto : FOF_fiber + (1|sessid) \quad (3)$$

986 where μ is $p(correct)$, *isopto* indicates whether the laser was on or off. *FOF_fiber*
987 indicates whether the fiber was plugged into bilateral FOF or Sham. *sessid* is the session
988 ID as factors. This model was fitted seperately for each task (egocentric/allocentric/allocentric-
989 reduced task) and laser timing condition (laser on for cue or delay epoch). We regarded
990 this model as the full model *mf* (Equation 3). To check sailencing effects on the animals'
991 performance, we drop the interaction between *isopto* and *FOF_fiber* from the fixed
992 effects and fit a reduced model *mr* (Equation 4) as follows:

$$\mu \sim 0 + isopto + FOF_fiber + (1|sessid) \quad (4)$$

993 The likelihood ratio test was performed using *lrtest(mf, mr)* (from the lmtest R
994 package) to determine whether the treatment had a significant effect on the animals'
995 performance.

996 For the optogenetic sailencing effect comparison between allocentric and egocentric
997 task,

$$\mu \sim 0 + ego_task + isopto + isopto : FOF_fiber : ego_task + (1|subj_id/sessid) \quad (5)$$

998 where μ is $p(correct)$, *isopto* indicates whether the laser was on or off. *FOF_fiber*
999 indicates whether the fiber was plugged into bilateral FOF or Sham. *ego_task* indicates
1000 whether the session was egocentric or allocentric task. *sessid* is the session ID as factors.
1001 *subj_id* is the subject ID as factors. We regarded this model as the full model *mf*
1002 (Equation 5). Similiarly, to determine whether the sailencing effect was different between

1003 allocentric and egocentric task, we drop *ego_task* from the interaction term from the
 1004 fixed effects and fit a reduced model *mr* (Equation 6) as follows:

$$\mu \sim 0 + \text{ego_task} + \text{isopto} + \text{isopto : FOF_fiber} + (1|\text{subjid}/\text{sessid}) \quad (6)$$

1005 The likelihood ratio test was performed using *lrtest(mf, mr)* (from the lmtest R
 1006 package) to determine whether the sailencing effect was different between allocentric
 1007 and egocentric task.

1008 Similarly, the formula of the full model *mf* (Equation 7) and the reduced model *mr*
 1009 (Equation 8) for the comparision between allocentric task and allocentric-reduced task
 1010 was:

$$\mu \sim 0 + \text{full_task} + \text{isopto} + \text{isopto : FOF_fiber : full_task} + (1|\text{subjid}/\text{sessid}) \quad (7)$$

$$\mu \sim 0 + \text{full_task} + \text{isopto} + \text{isopto : FOF_fiber} + (1|\text{subjid}/\text{sessid}) \quad (8)$$

1011 where *full_task* indicates whether the session was allocentric task or the reduced version
 1012 of the allocentric task.

1013 **GLMM selection for quantifying the difference of FOF sailencing mod-
 1014 ulation between two tasks**

1015 The GLMM for task comparision (Equation 5) was picked from a sets of potential
 1016 models, based on the its fitting performance.

1017 **Synthetic data for optogenetics experiments** The verification and comparision
 1018 for different GLMMS were performed on the synthetic data which were known to have
 1019 laser modulation on FOF sailencing for the egocentric task, but not on the allocentric
 1020 task. To make sure the sructure of the synthetic data is match to the real data, we
 1021 had those considerations (1) The sample size was matched with the real data: it had
 1022 the same number of subject, sessions and trials. (2) Across-session variblity and across-
 1023 subject variblity was modeled as distrubitions with different μ (3) A small impairment
 1024 for egocentric task FOF sailencing was sampled from a distrubition.

1025 **Model comparisions with synthetic optogenetics data** We defined those nine
 1026 models for comparision (Equation 9 - 16). All modeleds shared a similar designed that
 1027 fit $p(\text{correct})$ (or μ , as a parameter from binomial distrubition) with a logistic function
 1028 of task, laser on/off, fiber location (bilateral FOF or sham). But different interaction
 1029 between those three terms were implemented to determin the potenail best way to
 1030 model those interactions. The variability for each sessions(nested into each subjects)
 1031 were modeled as random effect for all models.

$$\mu \sim 0 + \text{ego_task} + \text{isopto : FOF_fiber} + (1|\text{subjid}/\text{sessid}) \quad (9)$$

$$\mu \sim 0 + \text{ego_task} + \text{isopto} + \text{FOF_fiber} + (1|\text{subjid}/\text{sessid}) \quad (10)$$

$$\mu \sim 0 + \text{FOF_fiber} + \text{isopto} + \text{isopto : ego_task} + (1|\text{subjid}/\text{sessid}) \quad (11)$$

$$\mu \sim 0 + \text{ego_task} + \text{isopto} + \text{isopto : FOF_fiber} + (1|\text{subjid}/\text{sessid}) \quad (12)$$

$$\mu \sim 0 + \text{ego_task} : \text{isopto : FOF_fiber} + (1|\text{subjid}/\text{sessid}) \quad (13)$$

$$\mu \sim 0 + ego_task + isopto + isopto : FOF_fiber + isopto : ego_task + (1|subjid/sessid) \quad (14)$$

$$\mu \sim 0 + ego_task * isopto * FOF_fiber + (1|subjid/sessid) \quad (15)$$

$$\mu \sim 0 + \text{ego_task} + \text{isopto} + \text{isopto : FOF_fiber} + \text{isopto : FOF_fiber : ego_task} + (1 | \text{subjid} / \text{sessid}) \quad (16)$$

1040 where μ is *p(correct)*, *isopto* indicates whether the laser was on or off. *FOF_fiber*
 1041 indicates whether the fiber was plugged into bilateral FOF or Sham. *ego_task* indicates
 1042 whether the session was egocentric or allocentric task. *sessid* is the session ID as factors.
 1043 *subjID* is the subject ID as factors.

We calculated the Akaike information criterion(AIC) and Bayesian information criterion (BIC) for all models. The best model (Equation 16) was picked based on the lowest BIC and AIC quantification (Supplementary Figure 5b).

Dynamical Model

We developed a numerical model to elucidate how different forms of short-term memory (STM) may be recruited under varying task demands. The model have two parts: 1) selective excitation module, and 2) attractor networks. For two attractor modules, one was for maintaining a planned motor action (egocentric memory, denote as FOF) and another for storing the auditory cue (could also be the allocentric target position, denoted as X). Each of the attractor modules can exhibit persistent activity once selectively excited, enabling it to hold the relevant information over a delay period. To simplify the model, we only built an attractor model for FOF module but not the X. For X we always return the choice with certain correct rate. And we set X to store the auditory cue.

1058 Selective Excitation The module checks each attractor module’s net cost and pro-
1059 vides sufficient excitatory drive as to the attractor module with the more favorable
1060 trade-off. We denoted the excitation to FOF (w_{FOF} between 0 and 1) that determines
1061 the excitation that FOF received. Similarly, w_X denotes the excitation that region X
1062 receives. Following our neural findings, we defined the overall cost for the selective
1063 excitation module:

$$\text{cost}(w_{\text{EOF}}, w_{\text{X}}) = \mathcal{C}_{\text{X}} w_{\text{X}} + \mathcal{C}_{\text{EOF}} w_{\text{EOF}} \quad (17)$$

1064 Here C_X and C_{FOF} are the cost for using FOF or area X for short-term memory. The
 1065 cost of both area was defined as

$$\mathcal{C}_X = C_{\text{bits}}^X N^X \quad (18)$$

$$\mathcal{C}_{FOF} = C_{\text{bits}}^{FOF} N^{FOF} \quad (19)$$

1067 Here N^X and N^{FOF} was the number of bits to get stored in that brain area for the
 1068 short-term memory. In the ego task, FOF maintains a simple binary choice (left vs.
 1069 right, Supplementary Figure 1a, Left) which yeild $N^{FOF} = 1$. Meanwhile for the allo
 1070 task, FOF could maintains multiple possible target directions(Supplementary Figure 1a,
 1071 Right). We set $N^{FOF} = 4$ in this siuation for a larger amount of content to be stored
 1072 in the short-term memory. Finally, the auditory cue was always binary, therefore we set
 1073 $N^X = 1$ for both task.

¹⁰⁷⁴ C_{bits}^X were the bits of memory cost for region X (or region FOF). We set $C_{\text{bits}}^{FOF} = 0.3$
¹⁰⁷⁵ and $C_{\text{bits}}^X = 1$ to mimic the situation that FOF is prioritized for the short-term memory
¹⁰⁷⁶ of upcoming movement. We also set $w_X = 1 - w_{FOF}$ to further simplify the model.

1077 With all of those constants defined, the overall cost for the selective excitation module
 1078 can be written as:

$$\text{cost}(w_{\text{FOF}}) = \begin{cases} 1 - 0.7w_{\text{FOF}} & \text{task} = Ego \\ 1 + 0.4w_{\text{FOF}} & \text{task} = Allo \end{cases} \quad (20)$$

1079 For optimization, we defined the loss as:

$$L(w_{\text{FOF}}, w_X) = \text{cost}^2(w_{\text{FOF}}, w_X) \quad (21)$$

1080 Since we defined $w_X = 1 - w_{\text{FOF}}$, The learning trajectory of w_{FOF} takes the form

$$w_{\text{FOF}}^{(t+1)} = w_{\text{FOF}}^{(t)} - \alpha \frac{\partial}{\partial w_{\text{FOF}}} L(w_{\text{FOF}}) + \sigma_w \epsilon \quad (22)$$

1081 where α is the learning rate, ϵ represents white noise, and σ_w is a parameter controlling
 1082 noise amplitude. w_{FOF} values are clipped between 0 and 1 after each training iteration.
 1083 For completeness, we include the expressions for $\frac{\partial}{\partial w_{\text{FOF}}} L(w_{\text{FOF}})$:

$$\frac{\partial}{\partial w_{\text{FOF}}} L(w_{\text{FOF}}) = \begin{cases} 0.98w_{\text{FOF}} - 1.4 & \text{task} = Ego \\ 0.4w_{\text{FOF}} + 0.08 & \text{task} = Allo \end{cases} \quad (23)$$

1084 Network Model of FOF

1085 We modeled FOF/M2 as binary attractor network following previous work^{28,29}. We
 1086 use a Wilson-Cowan model of cortical interactions^{67,68} with two competing, mutually
 1087 inhibiting sub-populations, each coding for a different behavioural decision:

$$\tau \frac{dr_1}{dt} = -r_1 + F(E_{\text{EXT}}(t)w_{\text{FOF}} + I_1 + w_{\text{rec}}r_1 - w_{\text{inh}}r_2) + \sqrt{\tau}\sigma_r\epsilon_1 \quad (24)$$

$$\tau \frac{dr_2}{dt} = -r_2 + F(E_{\text{EXT}}(t)w_{\text{FOF}} + I_2 + w_{\text{rec}}r_2 - w_{\text{inh}}r_1) + \sqrt{\tau}\sigma_r\epsilon_2 \quad (25)$$

1088 where τ is the population rate time constant, r_i is the firing rate of population i , I_i task-specific input that indicates evidence in favour of decision 1 or 2, w_{rec} is the strength of recurrent connectivity within each region, w_{inh} is the strength with which populations 1 and 2 inhibit each other, ϵ_i are different realizations of white noise and σ_r is a parameter controlling noise amplitude. $F(x)$ is the activation function, defined as a generalized sigmoid: $F(x) = \frac{1}{1+\exp(-x)}$. $E_{\text{EXT}}(t) = f(t)$ is a linear ramping background excitatory input from 0 to 8 over the 1.5s time course. w_{FOF} is the gain from **Selective Excitation** module.

1097
 1098 We use Euler integration to solve equation dynamics, which taking into account the
 1099 stochastic term scales with time, results in:

$$r_i^{(t+1)} = r_i^{(t)} + \frac{1}{\tau} \left[-r_i^{(t)} + F(E_{\text{EXT}} + I_i^{(t)} + w_{\text{rec}}r_i^{(t)} - w_{\text{inh}}r_{j \neq i}^{(t)}) \right] dt + \frac{1}{\sqrt{\tau}}\sigma_r\epsilon_i\sqrt{dt} \quad (26)$$

1100 All parameters used in simulations during learning for the controller are included in
 1101 Table 1.

1102 For the simulation of optogenetics silencing of FOF during the delay period $t > 0.75s$,
 1103 we discounted $E_{\text{EXT}}(t)$:

$$E_{\text{EXT}}(t > 0.75) = 0.1E_{\text{EXT}}(t > 0.75) + 0.2 \quad (27)$$

Symbol	Description	Value
τ	Population rate time constant	0.1
I_i	Task-specific input	0.1 (wrong) / 0.15 (right)
w_{rec}	Strength of recurrent connectivity	1.1
w_{inh}	Inhibitory strength	4
σ_r	Noise amplitude parameter	0.005
dt	Discretized timestep	0.01

Table 1. Parameters of network model of FOF.

1104 Use of Large language model(LLM)

1105 Large Language Models (LLMs), including ChatGPT-3.5/4/4o and DeepSeek R1, were
1106 used to assist with programming tasks and writing refinement. For programming, we
1107 provided clear specifications for input/output data structures and the logic of specific
1108 small functions before using LLMs for code generation. All generated code was manually
1109 reviewed, tested, and validated before implementation.

1110 **References**

- 1111 [1] Cheng Wang, Xiaojing Chen, and James J Knierim. Egocentric and allocentric
1112 representations of space in the rodent brain. *Current Opinion in Neurobiology*, 60:
1113 12–20, February 2020. doi: 10.1016/j.conb.2019.11.005.
- 1114 [2] David Zipser and Richard A. Andersen. A back-propagation programmed network
1115 that simulates response properties of a subset of posterior parietal neurons. *Nature*,
1116 331(6158):679, February 1988. doi: 10.1038/331679a0.
- 1117 [3] Yale E. Cohen and Richard A. Andersen. A common reference frame for movement
1118 plans in the posterior parietal cortex. *Nature Reviews Neuroscience*, 3(7):553–562,
1119 July 2002. doi: 10.1038/nrn873.
- 1120 [4] Jacob M. Olson, Jamie K. Li, Sarah E. Montgomery, and Douglas A. Nitz. Sec-
1121 ondary Motor Cortex Transforms Spatial Information into Planned Action dur-
1122 ing Navigation. *Current Biology*, page S0960982220303547, April 2020. doi:
1123 10.1016/j.cub.2020.03.016.
- 1124 [5] Jeffrey C Erlich, Max Bialek, and Carlos D Brody. A cortical substrate for memory-
1125 guided orienting in the rat. *Neuron*, 72(2):330–343, October 2011. doi: 10.1016/j.
1126 neuron.2011.07.010.
- 1127 [6] Nuo Li, Kayvon Daie, Karel Svoboda, and Shaul Druckmann. Robust neuronal
1128 dynamics in premotor cortex during motor planning. *Nature*, 532(7600):459–464,
1129 April 2016. doi: 10.1038/nature17643.
- 1130 [7] Joshua I. Gold and Michael N. Shadlen. The Neural Basis of Decision Making.
1131 *Annual Review of Neuroscience*, 30(1):535–574, 2007. doi: 10.1146/annurev.neuro.
1132 29.051605.113038.
- 1133 [8] Hidehiko K. Inagaki, Susu Chen, Kayvon Daie, Arseny Finkelstein, Lorenzo
1134 Fontolan, Sandro Romani, and Karel Svoboda. Neural Algorithms and Circuits
1135 for Motor Planning. *Annual Review of Neuroscience*, 45(1):249–271, July 2022.
1136 doi: 10.1146/annurev-neuro-092021-121730.
- 1137 [9] Liujunli Li, Timo Flesch, Ce Ma, Jingjie Li, Yizhou Chen, Hung-Tu Chen, and
1138 Jeffrey C. Erlich. Encoding of 2D self-centered plans and world-centered positions
1139 in the rat frontal orienting field. *The Journal of Neuroscience*, page e0018242024,
1140 August 2024. doi: 10.1523/JNEUROSCI.0018-24.2024.
- 1141 [10] Amitai Shenhav, Matthew M. Botvinick, and Jonathan D. Cohen. The Expected
1142 Value of Control: An Integrative Theory of Anterior Cingulate Cortex Function.
1143 *Neuron*, 79(2):217–240, July 2013. doi: 10.1016/j.neuron.2013.07.007.
- 1144 [11] S. Funahashi, C. J. Bruce, and P. S. Goldman-Rakic. Mnemonic coding of visual
1145 space in the monkey’s dorsolateral prefrontal cortex. *Journal of Neurophysiology*,
1146 61(2):331–349, February 1989. doi: 10.1152/jn.1989.61.2.331.
- 1147 [12] Philip N Sabes. The planning and control of reaching movements. *Current Opin-
1148 ion in Neurobiology*, 10(6):740–746, December 2000. doi: 10.1016/S0959-4388(00)
1149 00149-5.

- 1150 [13] Krishna V. Shenoy, Maneesh Sahani, and Mark M. Churchland. Cortical Control
1151 of Arm Movements: A Dynamical Systems Perspective. *Annual Review of Neuro-*
1152 *science*, 36(1):337–359, July 2013. doi: 10.1146/annurev-neuro-062111-150509.
- 1153 [14] Matthew T. Kaufman, Mark M. Churchland, Stephen I. Ryu, and Krishna V.
1154 Shenoy. Cortical activity in the null space: Permitting preparation without move-
1155 ment. *Nature Neuroscience*, 17(3):440–448, March 2014. doi: 10.1038/nn.3643.
- 1156 [15] Zengcai V. Guo, Nuo Li, Daniel Huber, Eran Ophir, Diego Gutnisky, Jonathan T.
1157 Ting, Guoping Feng, and Karel Svoboda. Flow of Cortical Activity Underlying a
1158 Tactile Decision in Mice. *Neuron*, 81(1):179–194, January 2014. doi: 10.1016/j.
1159 *neuron*.2013.10.020.
- 1160 [16] Chunyu A. Duan, Yuxin Pan, Guofen Ma, Taotao Zhou, Siyu Zhang, and Ning-
1161 long Xu. A cortico-collicular pathway for motor planning in a memory-dependent
1162 perceptual decision task. *Nature Communications*, 12(1):2727, May 2021. doi:
1163 10.1038/s41467-021-22547-9.
- 1164 [17] Richard A. Andersen, Lawrence H. Snyder, Chiang-Shan Li, and Brigitte Stricanne.
1165 Coordinate transformations in the representation of spatial information. *Current
1166 Opinion in Neurobiology*, 3(2):171–176, April 1993. doi: 10.1016/0959-4388(93)
1167 90206-E.
- 1168 [18] Bijan Pesaran, Matthew J. Nelson, and Richard A. Andersen. Dorsal Premotor
1169 Neurons Encode the Relative Position of the Hand, Eye, and Goal during Reach
1170 Planning. *Neuron*, 51(1):125–134, July 2006. doi: 10.1016/j.neuron.2006.05.025.
- 1171 [19] Edvard I. Moser, Emilio Kropff, and May-Britt Moser. Place Cells, Grid Cells, and
1172 the Brain’s Spatial Representation System. *Annual Review of Neuroscience*, 31(1):
1173 69–89, July 2008. doi: 10.1146/annurev.neuro.31.061307.090723.
- 1174 [20] Kevin J. Miller, Matthew M. Botvinick, and Carlos D. Brody. Dorsal hippocampus
1175 contributes to model-based planning. *Nature Neuroscience*, July 2017. doi: 10.
1176 1038/nn.4613.
- 1177 [21] Jake Ormond and John O’Keefe. Hippocampal place cells have goal-oriented vector
1178 fields during navigation. *Nature*, 607(7920):741–746, July 2022. doi: 10.1038/
1179 s41586-022-04913-9.
- 1180 [22] David J.-N. Maisson, Roberto Lopez Cervera, Benjamin Voloh, Indirah Conover,
1181 Mrunal Zambre, Jan Zimmermann, and Benjamin Y. Hayden. Widespread coding
1182 of navigational variables in prefrontal cortex. *Current Biology*, 33(16):3478–3488.e3,
1183 August 2023. doi: 10.1016/j.cub.2023.07.024.
- 1184 [23] Aaron A. Wilber, Benjamin J. Clark, Tyler C. Forster, Masami Tatsuno, and
1185 Bruce L. McNaughton. Interaction of Egocentric and World-Centered Reference
1186 Frames in the Rat Posterior Parietal Cortex. *Journal of Neuroscience*, 34(16):
1187 5431–5446, April 2014. doi: 10.1523/JNEUROSCI.0511-14.2014.
- 1188 [24] Douglas A Nitz. Spaces within spaces: Rat parietal cortex neurons register position
1189 across three reference frames. *Nature Neuroscience*, 15(10):1365–1367, October
1190 2012. doi: 10.1038/nn.3213.

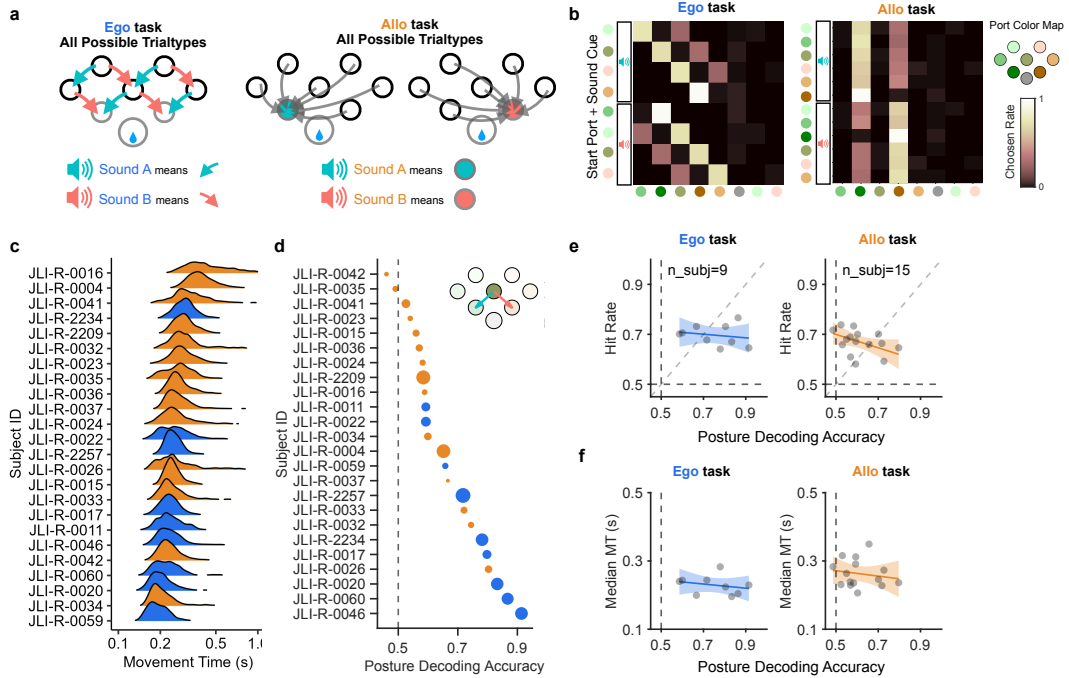
- 1191 [25] Cheng Wang, Xiaojing Chen, Heekyung Lee, Sachin S. Deshmukh, D. Yoga-
1192 narasimha, Francesco Savelli, and James J. Knierim. Egocentric coding of external
1193 items in the lateral entorhinal cortex. *Science*, 362(6417):945–949, November 2018.
1194 doi: 10.1126/science.aau4940.
- 1195 [26] Charles D Kopec, Jeffrey C Erlich, Bingni W Brunton, Karl Deisseroth, and Car-
1196 los D Brody. Cortical and Subcortical Contributions to Short- Term Memory
1197 for Orienting Movements. *Neuron*, 88(2):367–377, October 2015. doi: 10.1016/
1198 j.neuron.2015.08.033.
- 1199 [27] Zengcai V. Guo, Hidehiko K. Inagaki, Kayvon Daie, Shaul Druckmann, Charles R.
1200 Gerfen, and Karel Svoboda. Maintenance of persistent activity in a frontal thala-
1201 mocortical loop. *Nature*, 545(7653):181–186, May 2017. doi: 10.1038/nature22324.
- 1202 [28] Alex T. Piet, Jeffrey C. Erlich, Charles D. Kopec, and Carlos D. Brody. Rat
1203 Prefrontal Cortex Inactivations during Decision Making Are Explained by Bistable
1204 Attractor Dynamics. *Neural Computation*, 29(11):2861–2886, August 2017. doi:
1205 10.1162/neco_a_01005.
- 1206 [29] Hidehiko K. Inagaki, Lorenzo Fontolan, Sandro Romani, and Karel Svoboda. Dis-
1207 crete attractor dynamics underlies persistent activity in the frontal cortex. *Nature*,
1208 566(7743):212–217, February 2019. doi: 10.1038/s41586-019-0919-7.
- 1209 [30] Julie A. Charlton and Robbe L. T. Goris. Abstract deliberation by visuomotor
1210 neurons in prefrontal cortex. *Nature Neuroscience*, 27(6):1167–1175, June 2024.
1211 doi: 10.1038/s41593-024-01635-1.
- 1212 [31] Elise N. Mangin, Jian Chen, Jing Lin, and Nuo Li. Behavioral measurements of
1213 motor readiness in mice. *Current Biology*, 33(17):3610–3624.e4, September 2023.
1214 doi: 10.1016/j.cub.2023.07.029.
- 1215 [32] Ivan Voitov and Thomas D. Mrsic-Flogel. Cortical feedback loops bind distributed
1216 representations of working memory. *Nature*, 608(7922):381–389, August 2022. doi:
1217 10.1038/s41586-022-05014-3.
- 1218 [33] Chunyu A Duan, Jeffrey C Erlich, and Carlos D Brody. Requirement of Prefrontal
1219 and Midbrain Regions for Rapid Executive Control of Behavior in the Rat. *Neuron*,
1220 86(6):1491–1503, June 2015. doi: 10.1016/j.neuron.2015.05.042.
- 1221 [34] Munib A. Hasnain, Jaclyn E. Birnbaum, Juan Luis Ugarte Nunez, Emma K. Hart-
1222 man, Chandramouli Chandrasekaran, and Michael N. Economo. Separating cogni-
1223 tive and motor processes in the behaving mouse. *Nature Neuroscience*, February
1224 2025. doi: 10.1038/s41593-024-01859-1.
- 1225 [35] Talmo D. Pereira, Nathaniel Tabris, Arie Matsliah, David M. Turner, Junyu Li,
1226 Shruthi Ravindranath, Eleni S. Papadoyannis, Edna Normand, David S. Deutsch,
1227 Z. Yan Wang, Grace C. McKenzie-Smith, Catalin C. Mitelut, Marielisa Diez Castro,
1228 John D’Uva, Mikhail Kislin, Dan H. Sanes, Sarah D. Kocher, Samuel S.-H. Wang,
1229 Annegret L. Falkner, Joshua W. Shaevitz, and Mala Murthy. SLEAP: A deep
1230 learning system for multi-animal pose tracking. *Nature Methods*, 19(4):486–495,
1231 April 2022. doi: 10.1038/s41592-022-01426-1.

- 1232 [36] Hidehiko K. Inagaki, Susu Chen, Margreet C. Ridder, Pankaj Sah, Nuo Li, Zidan
1233 Yang, Hana Hasanbegovic, Zhenyu Gao, Charles R. Gerfen, and Karel Svoboda.
1234 A midbrain-thalamus-cortex circuit reorganizes cortical dynamics to initiate move-
1235 ment. *Cell*, 185(6):1065–1081.e23, March 2022. doi: 10.1016/j.cell.2022.02.006.
- 1236 [37] Mathias Mahn, Lihi Gibor, Pritish Patil, Katayun Cohen-Kashi Malina, Shir Oring,
1237 Yoav Printz, Rivka Levy, Ilan Lampl, and Ofer Yizhar. High-efficiency optogenetic
1238 silencing with soma-targeted anion-conducting channelrhodopsins. *Nature Commu-*
1239 *nica*ns, 9(1):4125, October 2018. doi: 10.1038/s41467-018-06511-8.
- 1240 [38] Andrew Gelman and Hal Stern. The Difference Between “Significant” and “Not
1241 Significant” is not Itself Statistically Significant. *The American Statistician*, 60(4):
1242 328–331, November 2006. doi: 10.1198/000313006X152649.
- 1243 [39] Liping Yu, Jiawei Hu, Chenlin Shi, Li Zhou, Maozhi Tian, Jiping Zhang, and
1244 Jinghong Xu. The causal role of auditory cortex in auditory working memory.
1245 *eLife*, 10:e64457, April 2021. doi: 10.7554/eLife.64457.
- 1246 [40] Ariel Gilad, Yasir Gallero-Salas, Dominik Groos, and Fritjof Helmchen. Behavioral
1247 Strategy Determines Frontal or Posterior Location of Short-Term Memory in Neo-
1248 cortex. *Neuron*, 99(4):814–828.e7, August 2018. doi: 10.1016/j.neuron.2018.07.029.
- 1249 [41] Yasir Gallero-Salas, Shuting Han, Yaroslav Sych, Fabian F. Voigt, Balazs Lau-
1250 renency, Ariel Gilad, and Fritjof Helmchen. Sensory and Behavioral Components of
1251 Neocortical Signal Flow in Discrimination Tasks with Short-Term Memory. *Neuron*,
1252 109(1):135–148.e6, January 2021. doi: 10.1016/j.neuron.2020.10.017.
- 1253 [42] Rifqi O. Affan, Ian M. Bright, Luke N. Pemberton, Nathanael A. Cruzado, Ben-
1254 jamin B. Scott, and Marc W. Howard. Ramping dynamics in the frontal cortex
1255 unfold over multiple timescales during motor planning. *Journal of Neurophysiol-*
1256 *ogy*, 133(2):625–637, February 2025. doi: 10.1152/jn.00234.2024.
- 1257 [43] Js Taube, Ru Muller, and Jb Ranck. Head-direction cells recorded from the post-
1258 subiculum in freely moving rats. I. Description and quantitative analysis. *The Jour-*
1259 *nal of Neuroscience*, 10(2):420–435, February 1990. doi: 10.1523/JNEUROSCI.
1260 10-02-00420.1990.
- 1261 [44] Andrew S. Alexander, Jennifer C. Robinson, Chantal E. Stern, and Michael E.
1262 Hasselmo. Gated transformations from egocentric to allocentric reference frames
1263 involving retrosplenial cortex, entorhinal cortex, and hippocampus. *Hippocampus*,
1264 33(5):465–487, May 2023. doi: 10.1002/hipo.23513.
- 1265 [45] Jonathan R. Whitlock, Robert J. Sutherland, Menno P. Witter, May-Britt Moser,
1266 and Edvard I. Moser. Navigating from hippocampus to parietal cortex. *Proceedings*
1267 *of the National Academy of Sciences*, 105(39):14755–14762, September 2008. doi:
1268 10.1073/pnas.0804216105.
- 1269 [46] Jae-Hyun Kim, Kayvon Daie, and Nuo Li. A combinatorial neural code for long-
1270 term motor memory. *Nature*, 637(8046):663–672, January 2025. doi: 10.1038/
1271 s41586-024-08193-3.
- 1272 [47] David J. Freedman and John A. Assad. Experience-dependent representation of
1273 visual categories in parietal cortex. *Nature*, 443(7107):85–88, September 2006. doi:
1274 10.1038/nature05078.

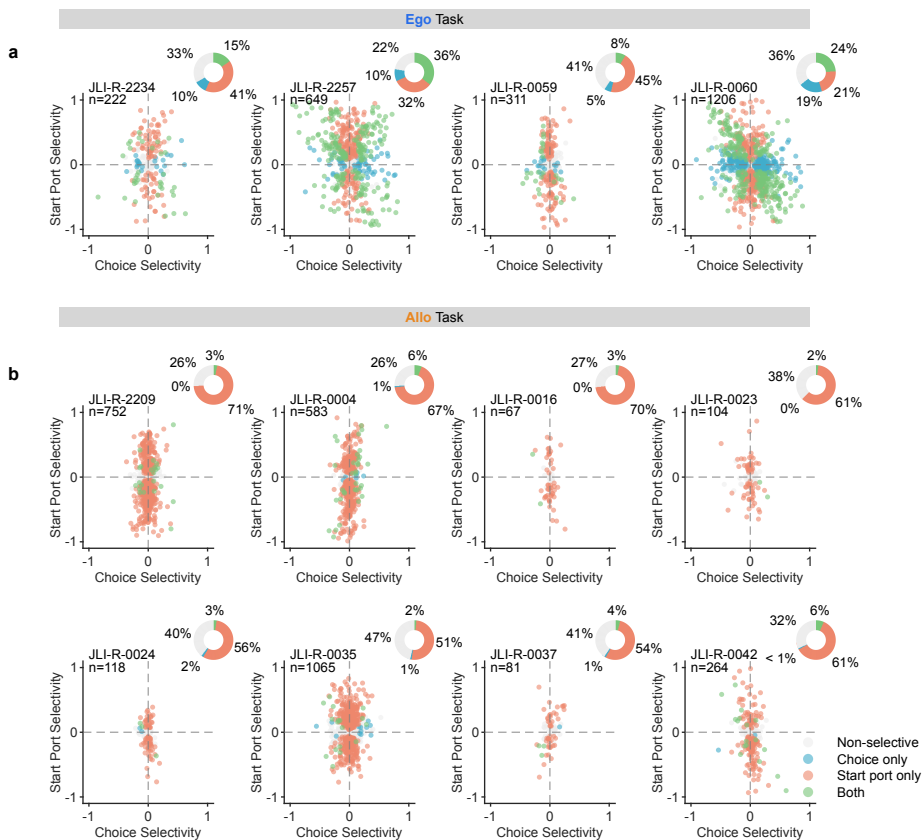
- 1275 [48] Kenneth W. Latimer and David J. Freedman. Low-dimensional encoding of decisions in parietal cortex reflects long-term training history. *Nature Communications*,
1276 14(1):1010, February 2023. doi: 10.1038/s41467-023-36554-5.
- 1278 [49] Hao Guo, Shenbing Kuang, and Alexander Gail. Sensorimotor environment
1279 but not task rule reconfigures population dynamics in rhesus monkey posterior
1280 parietal cortex. *Nature Communications*, 16(1):1116, February 2025. doi:
1281 10.1038/s41467-025-56360-5.
- 1282 [50] M Rushworth, M Walton, S Kennerley, and D Bannerman. Action sets and decisions
1283 in the medial frontal cortex. *Trends in Cognitive Sciences*, 8(9):410–417, September
1284 2004. doi: 10.1016/j.tics.2004.07.009.
- 1285 [51] F. A. Mansouri, M. J. Buckley, and K. Tanaka. The Essential Role of Primate
1286 Orbitofrontal Cortex in Conflict-Induced Executive Control Adjustment. *Journal
1287 of Neuroscience*, 34(33):11016–11031, August 2014. doi: 10.1523/JNEUROSCI.
1288 1637-14.2014.
- 1289 [52] Farshad A. Mansouri, Kenji Matsumoto, and Keiji Tanaka. Prefrontal Cell Activi-
1290 ties Related to Monkeys' Success and Failure in Adapting to Rule Changes in a
1291 Wisconsin Card Sorting Test Analog. *The Journal of Neuroscience*, 26(10):2745–
1292 2756, March 2006. doi: 10.1523/JNEUROSCI.5238-05.2006.
- 1293 [53] Adrian G Bondy, Julie A Charlton, Thomas Zhihao Luo, Charles D Kopec,
1294 Wynne M Stagnaro, Sarah Jo C Venditto, Laura Lynch, Sanjeev Janarthanan,
1295 Stefan N Oline, Timothy D Harris, and Carlos D Brody. Coordinated cross-brain
1296 activity during accumulation of sensory evidence and decision commitment, August
1297 2024.
- 1298 [54] James J. Jun, Nicholas A. Steinmetz, Joshua H. Siegle, Daniel J. Denman, Marius
1299 Bauza, Brian Barbarits, Albert K. Lee, Costas A. Anastassiou, Alexandru Andrei,
1300 Çağatay Aydin, Mladen Barbic, Timothy J. Blanche, Vincent Bonin, João Couto,
1301 Barundeb Dutta, Sergey L. Gratiy, Diego A. Gutnisky, Michael Häusser, Bill Karsh,
1302 Peter Ledochowitsch, Carolina Mora Lopez, Catalin Mitelut, Silke Musa, Michael
1303 Okun, Marius Pachitariu, Jan Putzeys, P. Dylan Rich, Cyrille Rossant, Wei-lung
1304 Sun, Karel Svoboda, Matteo Carandini, Kenneth D. Harris, Christof Koch, John
1305 O'Keefe, and Timothy D. Harris. Fully integrated silicon probes for high-density
1306 recording of neural activity. *Nature*, 551(7679):232–236, November 2017. doi: 10.
1307 1038/nature24636.
- 1308 [55] Jeffrey Erlich, Josh Moller-Mara, and Jingjie Li. Erlichlab/elutils: First Zenodo
1309 Release. Zenodo, May 2021.
- 1310 [56] Mihály Vöröslakos, Peter C Petersen, Balázs Vöröslakos, and György Buzsáki.
1311 Metal microdrive and head cap system for silicon probe recovery in freely mov-
1312 ing rodent. *eLife*, 10:e65859, May 2021. doi: 10.7554/eLife.65859.
- 1313 [57] Marius Pachitariu, Nicholas Steinmetz, Shabnam Kadir, Matteo Carandini, and
1314 Harris Kenneth D. Kilosort: Realtime spike-sorting for extracellular electrophysi-
1315 ology with hundreds of channels, June 2016.

- 1316 [58] Marius Pachitariu, Shashwat Sridhar, Jacob Pennington, and Carsen Stringer.
1317 Spike sorting with Kilosort4. *Nature Methods*, 21(5):914–921, May 2024. doi:
1318 10.1038/s41592-024-02232-7.
- 1319 [59] Xiaoxuan Jia, Joshua H. Siegle, Corbett Bennett, Samuel D. Gale, Daniel J. Den-
1320 man, Christof Koch, and Shawn R. Olsen. High-density extracellular probes reveal
1321 dendritic backpropagation and facilitate neuron classification. *Journal of Neuro-
1322 physiology*, 121(5):1831–1847, May 2019. doi: 10.1152/jn.00680.2018.
- 1323 [60] D. Mayerich, L. Abbott, and B. McCORMICK. Knife-edge scanning microscopy
1324 for imaging and reconstruction of three-dimensional anatomical structures of the
1325 mouse brain. *Journal of Microscopy*, 231(1):134–143, July 2008. doi: 10.1111/j.
1326 1365-2818.2008.02024.x.
- 1327 [61] Timothy Ragan, Lolahon R Kadiri, Kannan Umadevi Venkataraju, Karsten
1328 Bahlmann, Jason Sutin, Julian Taranda, Ignacio Arganda-Carreras, Yongsoo Kim,
1329 H Sebastian Seung, and Pavel Osten. Serial two-photon tomography for automated
1330 ex vivo mouse brain imaging. *Nature Methods*, 9(3):255–258, March 2012. doi:
1331 10.1038/nmeth.1854.
- 1332 [62] J-R. King and S. Dehaene. Characterizing the dynamics of mental representations:
1333 The temporal generalization method. *Trends in Cognitive Sciences*, 18(4):203–210,
1334 April 2014. doi: 10.1016/j.tics.2014.01.002.
- 1335 [63] Mike X Cohen. *Analyzing Neural Time Series Data: Theory and Practice*. The
1336 MIT Press, January 2014. doi: 10.7551/mitpress/9609.001.0001.
- 1337 [64] M. Pagan and N. C. Rust. Dynamic Target Match Signals in Perirhinal Cortex
1338 Can Be Explained by Instantaneous Computations That Act on Dynamic Input
1339 from Inferotemporal Cortex. *Journal of Neuroscience*, 34(33):11067–11084, August
1340 2014. doi: 10.1523/JNEUROSCI.4040-13.2014.
- 1341 [65] Chunyu A. Duan, Marino Pagan, Alex T. Piet, Charles D. Kopec, Athena Akrami,
1342 Alexander J. Riordan, Jeffrey C. Erlich, and Carlos D. Brody. Collicular circuits
1343 for flexible sensorimotor routing. *Nature Neuroscience*, 24(8):1110–1120, August
1344 2021. doi: 10.1038/s41593-021-00865-x.
- 1345 [66] Chaofei Bao, Xiaoyue Zhu, Joshua Möller-Mara, Jingjie Li, Sylvain Dubroqua, and
1346 Jeffrey C. Erlich. The rat frontal orienting field dynamically encodes value for
1347 economic decisions under risk. *Nature Neuroscience*, 26(11):1942–1952, November
1348 2023. doi: 10.1038/s41593-023-01461-x.
- 1349 [67] H. R. Wilson and J. D. Cowan. A mathematical theory of the functional dynamics
1350 of cortical and thalamic nervous tissue. *Kybernetik*, 13(2):55–80, September 1973.
1351 doi: 10.1007/BF00288786.
- 1352 [68] Alain Destexhe and Terrence J. Sejnowski. The Wilson–Cowan model, 36
1353 years later. *Biological Cybernetics*, 101(1):1–2, July 2009. doi: 10.1007/
1354 s00422-009-0328-3.

Supplementary

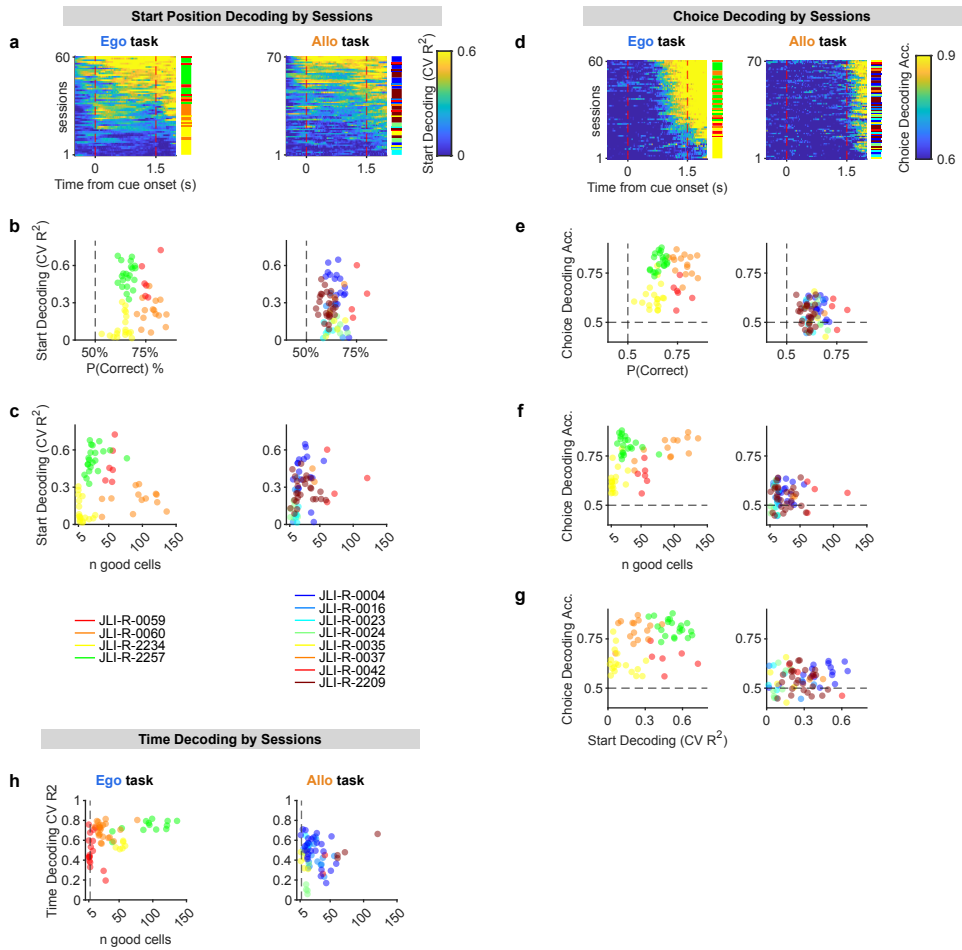


Supplementary Figure 1. Details for Animal's Choice, Movement Time and Posture Planning. **a.** Available trialtypes for each tasks. The "Ego" task had 5 different start ports and 8 different movement trajectories given different start port and auditory cues. All movement trajectories were either leftward or rightward for 45 deg downward, yielding only two possible movement directions. The "Allo" task had 7 different start ports and 10 different movement trajectories. **b.** Choice histogram for each trial-type for the "Ego" task (Left) and the "Allo" task (Right). Y-axis: trial-type, sort by start position (colored dots) and auditory cue (colored rectangle), X-axis: chosen port. Color means the proportion of hitting the given port in each trial-type. **c.** Distribution of movement times (MT) for each individual rat (For center port started trials, time between center port withdraw to choice port entry, hit trials only.). Orange: Allo animals; Blue: Ego animals. **d.** Decoding accuracy for choice from posture angle features (at $t=1.3$ s after trial onset) for each individual rat (Grey dots). Only selected centered port started trials. Dot size indicates the number of trials. **e.** The correlation between posture decoding accuracy and hit rate, for Ego task (Left) or Allo task (Right). Lines are Total Least Square(TLS) fit. Shaded areas are for 95% C.I. **f.** The correlation between posture decoding accuracy and movement time for each individual rats (grey dots), for Ego task (Left) or Allo task (Right). Lines are Total Least Square(TLS) fit. Shaded areas are for 95% C.I.

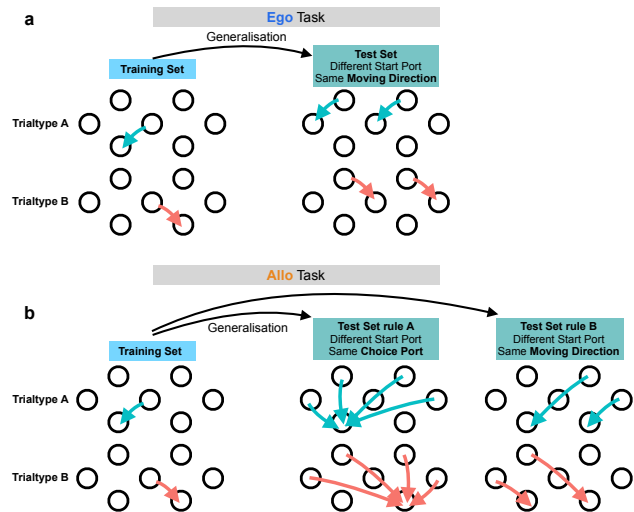


Supplementary Figure 2. Distribution of single-neuron selectivity indices across subjects.

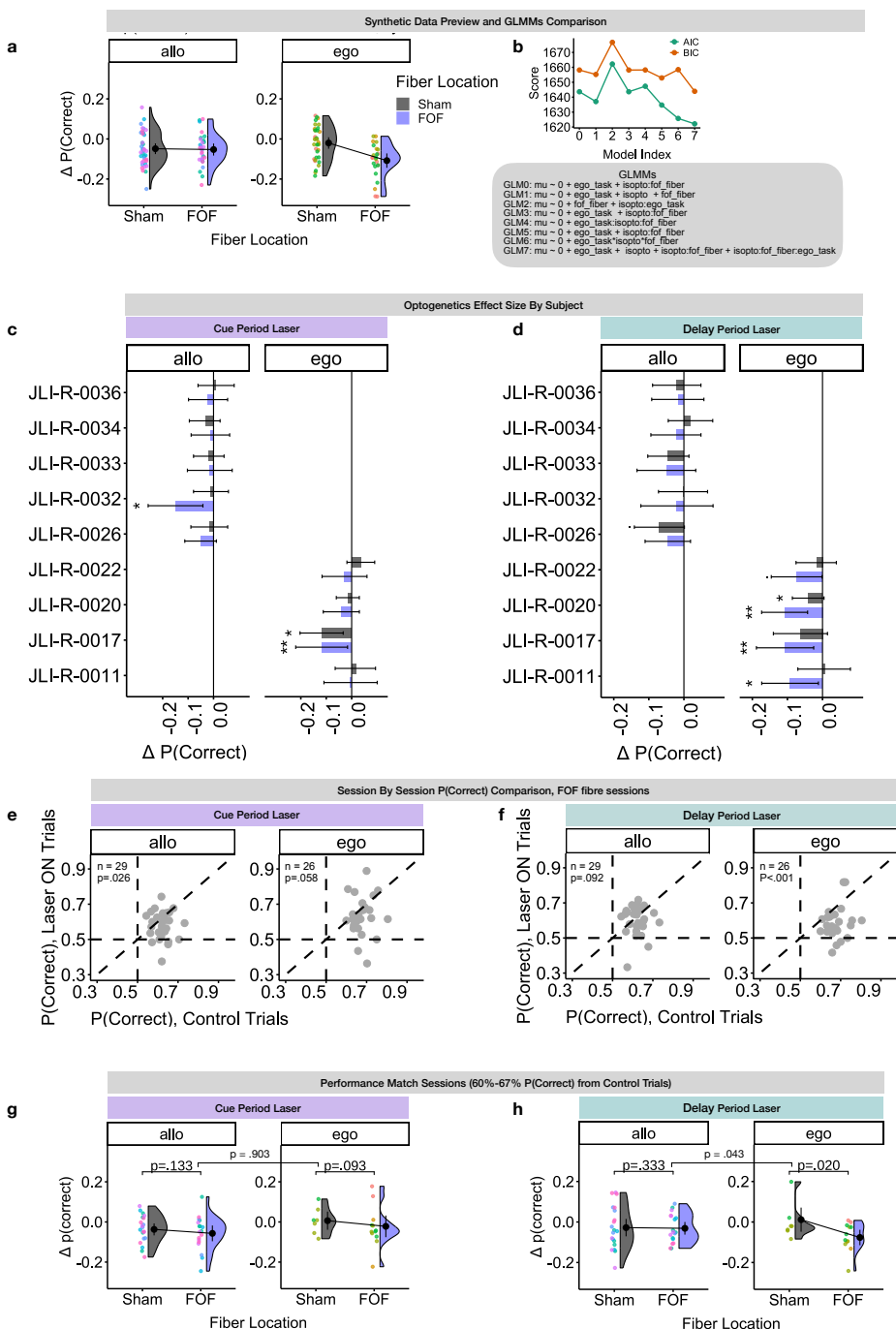
a. Scatter plot showing the distribution of selectivity indices for individual neurons recorded from each rat performing the Ego task. Each dot represents a single neuron, with its position reflecting selectivity for upcoming choice (x-axis) and start port position (y-axis), corresponding to analyses in Figure 2d. **b.** Same as (a), but for the Allo task, corresponding to Figure 2h. Pie plots next to each panel summarize the proportions of neurons classified as non-selective (gray), choice-selective only (blue), start port-selective only (orange), or selective for both (purple).



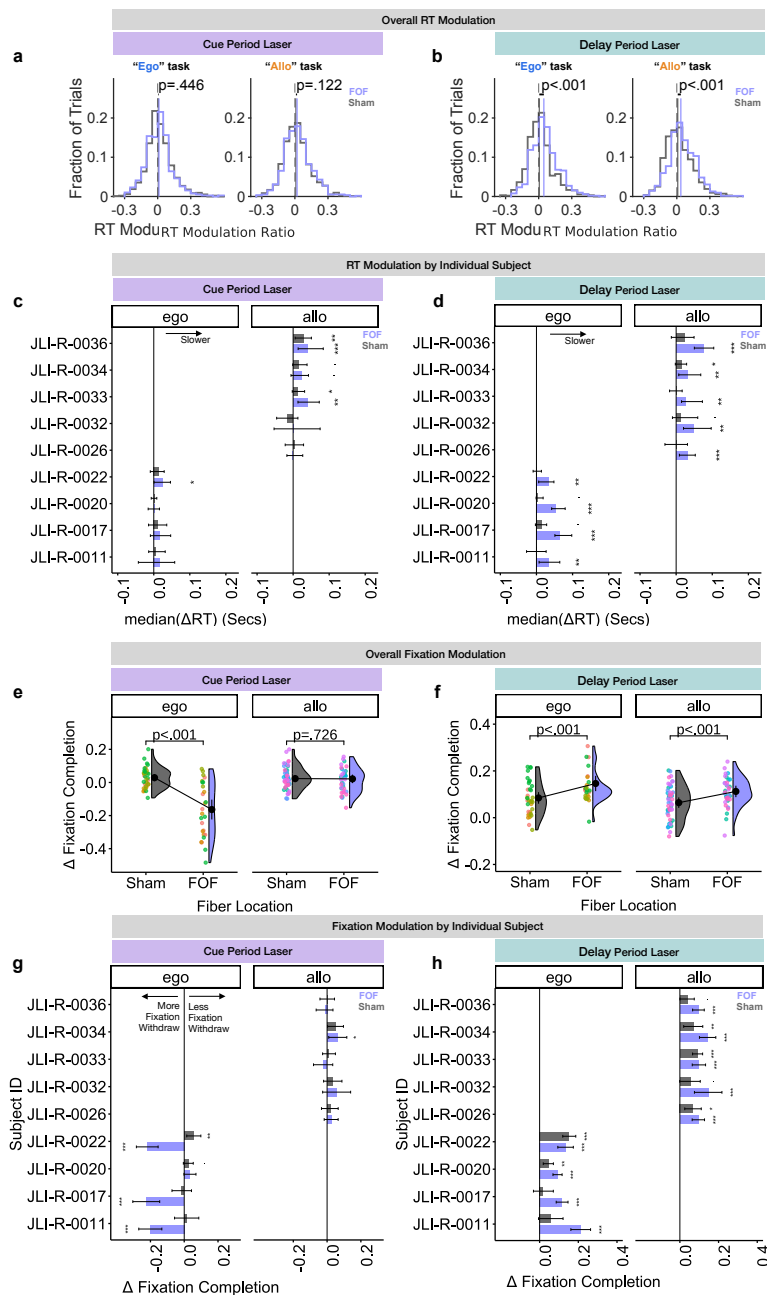
Supplementary Figure 3. Session-wise decoding performance for start position, choice, and time across subjects. **a, d.** Heatmaps showing session-wise decoding performance for start position (**a**) and choice (**d**) in the Ego (left panel) and Allo (right panel) tasks. Each row represents a session, with color reflecting decoding performance ($CV R^2$ for start position and CV % for choice decoding). Sessions are ordered based on the center of mass of decoding performance (calculated as the dot product between time and decoding performance). The color bar adjacent to each heatmap indicates the subject identity for each session, consistent with the color legend shown below. **b, e.** Scatter plots showing the relationship between decoding performance (start decoding in **b**, choice decoding in **e**) and behavioral performance, measured as the percentage of correct trials for each session. Each point represents a session, color-coded by subject. **c, f.** Decoding performance (start in **c**, choice in **f**) as a function of the number of good cells recorded per session, determined by quality metrics (see *Methods*). **g.** Relationship between start position decoding performance ($CV R^2$) and choice decoding performance ($CV \%$) across sessions. The dashed lines represent chance-level performance thresholds (50% for choice decoding). **h.** Time decoding performance ($CV R^2$) plotted against the number of good cells for Ego and Allo tasks. Each point in the scatter plots corresponds to an individual session, color-coded by subject. Each point in the scatter plots corresponds to an individual session, color-coded by subject. The dashed lines represent chance-level performance thresholds (50% for choice decoding and choice P(Correct)), except in **h**, where it indicates the inclusion threshold based on cell count for a comparison in Figure 5j.



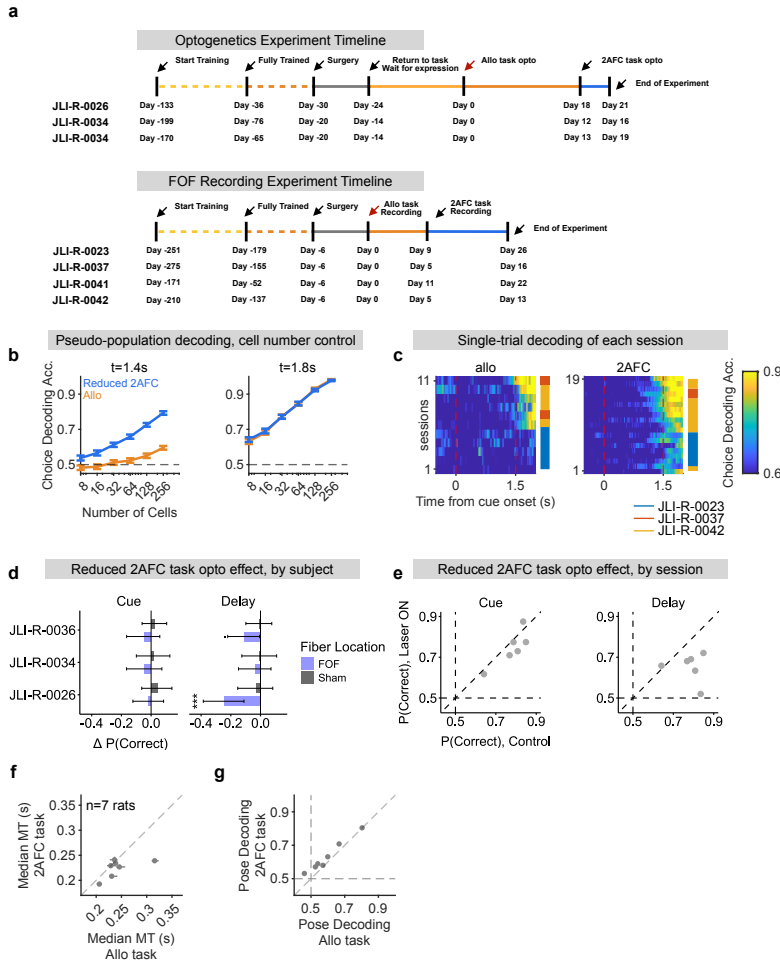
Supplementary Figure 4. Trialtype details for decoding generalization analysis **a.** for the Ego task, MidC port started trials were selected for the training set (Left) and other trials started from other ports but moved to the same direction were selected as test set (Right). Decoding results were shown in Figure 3l and Figure 3n. **b.** for the Allo task, MidC port started trials were selected for the training set (Left). In rule A, trials started from other ports but moved to the same choice port were selected as test set (Middle), decoding results were shown in Figure 3m (Left) and Figure 3o (Left). In rule B, trials started from other ports but moved toward the same directions were selected as test set (Right), decoding results were shown in Figure 3m (Right) and Figure 3o (Right).



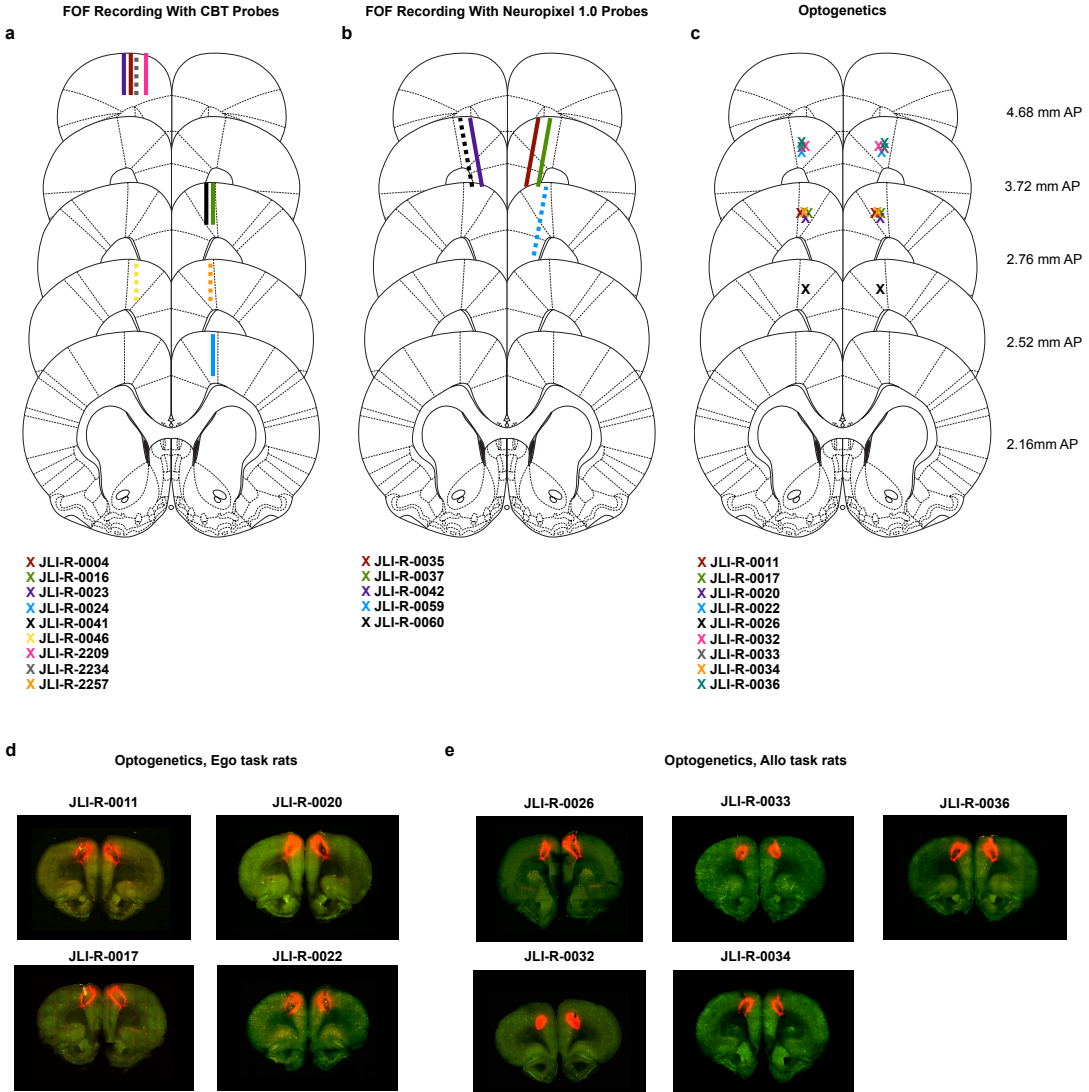
Supplementary Figure 5. Control analysis for FOF silencing **a**. Synthetic data that simulated opto modulation for some animals and sessions with performance variation for the "Ego" (left) and "Allo" (right) task. Y axis: fraction of correct choices for laser on trials - laser off trials for each session. X axis: fraction of correct choices for laser off trials. Y-axis: fraction of correct choices for laser on trials. P-value are from paired t-test. **b**. Same as **c**. **e**. Performance modulation for cue period laser effect for each sessions (FOF sessions only). Each dots are for individual sessions. X-axis: fraction of correct choices for laser off trials. Y-axis: fraction of correct choices for laser on trials. P-value are from paired t-test. **f**. Same as **e** but for delay period laser. **g**. Effects of cue period laser effect on behavior in the "Ego" task (Left) and the "Allo" task (Right) for sessions within 60-67% performance range in both tasks. Same as **a**. **h**. Same as **g** but for delay period laser effect.



Supplementary Figure 6. Response time (RT) and early fixation withdraw modulation with FOF silencing. RT was defined as the duration of the period starting upon the end of 1.5s fixation period, and ending upon choice port entry. Early fixation withdraw was defined as exiting from start port before the end of 1.5s fixation period. We quantified fixation completion rate as the fraction of trials that didn't have early withdraw. **a.** The distribution of RT change for cue period laser ON trials. The RT for each laser ON trials was normalized by the median of laser OFF trials of each session/trialtype/fiber and then transformed to log scale for "RT modulation ratio". Dash vertical line highlighted 0 for the X-axis. Grey and purple line indicated the median of RT modulation ratio for sham fiber trials and FOF fiber trials, respectively. **b.** The distribution of RT change for delay period laser ON trials, same as **a.** **c.** RT modulation for cue period FOF laser effect for each animals. Y-axis: individual animals, X-axis: median of RT for laser on trials - laser off trials for each session/trialtype/fiber. Error bars are 95% C.I. (bootstrap). Purple: FOF sessions; Grey: Sham sessions. **d.** RT modulation for delay period laser effect for each animals. Same as **c.** **e.** Effects of cue period laser effect on fixation completion rate. Y axis: fraction of fixation completion rate for laser on trials - laser off trials for each session (dots, colored by different animals). **f.** Same as **e.** but for delay period laser effect. **g.** fixation completion rate modulation for cue period laser effect for each animals. Y-axis: individual animals, X-axis: fixation completion rate for laser on trials - laser off trials for each session. Error bars are 95% C.I. (bootstrap). Purple: FOF sessions; Grey: Sham sessions. **h.** fixation completion rate modulation for delay period laser effect for each animals. Same as **g**



Supplementary Figure 7. Details for task transformation. **a.** Experimental timeline for each subject, showing the sequence of sessions during the Allo and reduced 2AFC tasks with optogenetic manipulations and electrophysiological recording experiments. Each row represents an individual subject. **b.** Pseudo-population decoding accuracy for choice as a function of the number of cells included in the pseudo-decoding model, comparing performance between the Allo and reduced 2AFC tasks. Decoding was performed at two key time points ($t = 1.4$ s during delay period and $t = 1.8$ s during the movement period). Errorbars indicate SEM. The horizontal dashed lines represent chance-level decoding thresholds. **c.** Session-wise heatmaps of choice decoding accuracy from electrophysiological data for the Allo (left) and reduced 2AFC (right) task. Each row represents a session, and color intensity reflects cross-validated decoding accuracy over time, aligned to cue onset. Sessions are sorted by the center of mass of decoding accuracy. The color bar adjacent to each heatmap indicates the subject identity for each session, consistent with the color legend shown below. **d.** Optogenetic silencing effects on task performance ($\Delta P(\text{Correct})$) for individual subjects during the cue (left) and delay period (right), for the reduced 2AFC task. Each row represents a subject, and error bars indicate 95% confidence intervals estimated from bootstrap resampling. **e.** FOF optogenetic effects by each session in reduced 2AFC task. Each dot represents a session. X-axis: $P(\text{Correct})$ for control trials, Y-axis: $P(\text{Correct})$ for cue period laser on trials (Left) or delay period laser on trials (Right). The horizontal and vertical dashed lines represent chance-level performance thresholds. **f.** Comparison of median movement times (MT) for each subject before and after task transformation from the Allo to the reduced 2AFC task. Each dot represents an individual subject. **g.** Comparison of posture decoding accuracy at $t=1.3$ s after cue onset (during late-delay period) for each subject before and after task transformation from the Allo to the reduced 2AFC task. Each dot represents an individual subject. The horizontal and vertical dashed lines represent chance-level decoding thresholds.



Supplementary Figure 8. Histology results. **a.** Reconstructed probe track for each rat that implanted cambrdige neurotech silicon probes in FOF. Solid line for the Allo task, dash line for the Ego task. **b.** Reconstructed probe track for each rat that implanted Neuropixel 1.0 probes in FOF. Solid line for the Allo task, dash line for the Ego task. **c.** Reconstructed optic fiber track for each rat with optogenetics surgery in bilateral FOF. **d.** Histology image for each rat from optogenetics experiment, in the Ego task. **e.** Histology image for each rat from optogenetics experiment, in the Allo task.

Supplementary Table 1. Experiment type for all subjects, CNT - Cambridge Neurotech probs

subjid	stain	gender	task	experiment
JLI-R-2209	Sprague-Dawley	M	Allo	Ephys Recording, CNT probe
JLI-R-2234	Sprague-Dawley	M	Ego	Ephys Recording, CNT probe
JLI-R-2257	Sprague-Dawley	M	Ego	Ephys Recording, CNT probe
JLI-R-0004	Lister-Hooded	M	Allo	Ephys Recording, CNT probe
JLI-R-0011	Lister-Hooded	M	Ego	Optogenetics
JLI-R-0015	Lister-Hooded	M	Allo	Ephys Recording, CNT probe
JLI-R-0016	Lister-Hooded	M	Allo	Ephys Recording, CNT probe
JLI-R-0017	Lister-Hooded	M	Ego	Optogenetics
JLI-R-0020	Lister-Hooded	M	Ego	Optogenetics
JLI-R-0022	Lister-Hooded	M	Ego	Optogenetics
JLI-R-0023	Lister-Hooded	M	Allo	Ephys Recording, CNT probe
JLI-R-0024	Lister-Hooded	M	Allo	Ephys Recording, CNT probe
JLI-R-0026	Lister-Hooded	M	Allo	Optogenetics
JLI-R-0032	Lister-Hooded	M	Allo	Optogenetics
JLI-R-0033	Lister-Hooded	M	Allo	Optogenetics
JLI-R-0034	Lister-Hooded	M	Allo	Optogenetics
JLI-R-0035	Lister-Hooded	M	Allo	Ephys Recording, Neuropixel 1.0
JLI-R-0036	Lister-Hooded	M	Allo	Optogenetics
JLI-R-0037	Lister-Hooded	F	Allo	Ephys Recording, Neuropixel 1.0
JLI-R-0041	Lister-Hooded	M	Allo	Ephys Recording, CNT probe
JLI-R-0042	Lister-Hooded	M	Allo	Ephys Recording, Neuropixel 1.0
JLI-R-0046	Lister-Hooded	F	Ego	Ephys Recording, CNT probe
JLI-R-0059	Lister-Hooded	M	Ego	Ephys Recording, Neuropixel 1.0
JLI-R-0060	Lister-Hooded	M	Ego	Ephys Recording, Neuropixel 1.0

1356 Statistic Table for Optogenetics Experiment

1357 1 Stats Test

1358 1.1 Figure 1

1359 1.1.1 Figure 1e, Hit Trials

1360 Likelihood ratio test

1361

1362 Model 1: logMT ~ 1 + task + (1 | subjid)

1363 Model 2: logMT ~ 1 + (1 | subjid)

1364 #Df LogLik Df Chisq Pr(>Chisq)

1365 1 4 26707

1366 2 3 26710 -1 5.0587 0.0245 *

1367 ---

1368 Signif. codes: 0 ‘*’ 0.001 ‘**’ 0.01 ‘*’ 0.05 ‘.’ 0.1 ‘ ’ 1**

1369 1.1.2 Figure 1e, Error Trials

1370 Likelihood ratio test

```

1371
1372 Model 1: logMT ~ 1 + task + (1 | subjid)
1373 Model 2: logMT ~ 1 + (1 | subjid)
1374 #Df LogLik Df Chisq Pr(>Chisq)
1375 1 4 10473
1376 2 3 10476 -1 5.2658 0.02175 *
1377 ---
1378 Signif. codes: 0 '***' 0.001 '**' 0.01 '*' 0.05 '.' 0.1 ' ' 1

```

1379 1.2 Figure 4

1380 1.2.1 Figure 4C, Left Panel, Ego task, Sham/FOF comparision

```

1381 Likelihood ratio test
1382
1383 Model 1: mu ~ 0 + isopto + fof_fiber + (1 | sessid)
1384 Model 2: mu ~ 0 + isopto + fof_fiber + isopto:fof_fiber + (1 | sessid)
1385 #Df LogLik Df Chisq Pr(>Chisq)
1386 1 3 -472.40
1387 2 4 -470.07 1 4.6549 0.03097 *
1388 ---
1389 Signif. codes: 0 '***' 0.001 '**' 0.01 '*' 0.05 '.' 0.1 ' ' 1

```

1390 1.2.2 Figure 4C, Right Panel, Allo task, Sham/FOF comparision

```

1391 Likelihood ratio test
1392
1393 Model 1: mu ~ 0 + isopto + fof_fiber + (1 | sessid)
1394 Model 2: mu ~ 0 + isopto + fof_fiber + isopto:fof_fiber + (1 | sessid)
1395 #Df LogLik Df Chisq Pr(>Chisq)
1396 1 3 -441.03
1397 2 4 -439.01 1 4.0364 0.04453 *
1398 ---
1399 Signif. codes: 0 '***' 0.001 '**' 0.01 '*' 0.05 '.' 0.1 ' ' 1

```

1400 1.2.3 Figure 4C, Main Comparision Between allo/ego task

```

1401 Likelihood ratio test
1402
1403 Model 1: mu ~ 0 + ego_task + isopto + isopto:fof_fiber + isopto:fof_fiber:ego_task +
1404 (1 | subjid/sessid)
1405 Model 2: mu ~ 0 + ego_task + isopto + isopto:fof_fiber + isopto:fof_fiber +
1406 (1 | subjid/sessid)
1407 #Df LogLik Df Chisq Pr(>Chisq)
1408 1 6 -776.33
1409 2 5 -776.49 -1 0.324 0.5692

```

1410 1.2.4 Figure 4D, Left Panel, Ego task, Sham/FOF comparision

```

1411 Likelihood ratio test
1412

```

```

1413 Model 1: mu ~ 0 + isopto + fof_fiber + (1 | sessid)
1414 Model 2: mu ~ 0 + isopto + fof_fiber + isopto:fof_fiber + (1 | sessid)
1415   #Df LogLik Df Chisq Pr(>Chisq)
1416   1   3 -478.16
1417   2   4 -473.39  1 9.5406    0.00201 **
1418   ---
1419 Signif. codes:  0 '***' 0.001 '**' 0.01 '*' 0.05 '.' 0.1 ' ' 1

```

1420 1.2.5 Figure 4D, Right Panel, Allo task, Sham/FOF comparision

```

1421 Likelihood ratio test
1422
1423 Model 1: mu ~ 0 + isopto + fof_fiber + (1 | sessid)
1424 Model 2: mu ~ 0 + isopto + fof_fiber + isopto:fof_fiber + (1 | sessid)
1425   #Df LogLik Df Chisq Pr(>Chisq)
1426   1   3 -445.28
1427   2   4 -444.51  1 1.5456    0.2138

```

1428 1.2.6 Figure 4D, Main Comparision Between allo/ego task

```

1429 Likelihood ratio test
1430
1431 Model 1: mu ~ 0 + ego_task + isopto + isopto:fof_fiber + isopto:fof_fiber:ego_task +
1432   (1 | subjid/sessid)
1433 Model 2: mu ~ 0 + ego_task + isopto + isopto:fof_fiber + isopto:fof_fiber +
1434   (1 | subjid/sessid)
1435   #Df LogLik Df Chisq Pr(>Chisq)
1436   1   6 -786.52
1437   2   5 -790.51 -1 7.9718    0.004751 **
1438   ---
1439 Signif. codes:  0 '***' 0.001 '**' 0.01 '*' 0.05 '.' 0.1 ' ' 1

```

1440 1.3 Figure 6

1441 1.3.1 Figure 6C hit trials

```

1442 Likelihood ratio test
1443
1444 Model 1: logMT ~ 1 + task + (1 | subjid)
1445 Model 2: logMT ~ 1 + (1 | subjid)
1446   #Df LogLik Df Chisq Pr(>Chisq)
1447   1   4 4295.2
1448   2   3 4209.3 -1 171.99 < 2.2e-16 ***
1449   ---
1450 Signif. codes:  0 '***' 0.001 '**' 0.01 '*' 0.05 '.' 0.1 ' ' 1

```

1451 1.3.2 Figure 6C error trials

```

1452 Likelihood ratio test
1453
1454 Model 1: logMT ~ 1 + task + (1 | subjid)

```

```

1455 Model 2: logMT ~ 1 + (1 | subjid)
1456     #Df LogLik Df Chisq Pr(>Chisq)
1457 1    4 961.48
1458 2    3 942.99 -1 36.982  1.192e-09 ***
1459 ---
1460 Signif. codes:  0 '***' 0.001 '**' 0.01 '*' 0.05 '.' 0.1 ' ' 1

```

1461 1.3.3 Figure 6D, Left Panel, Allo task, Sham/FOF comparision

```

1462 Likelihood ratio test
1463
1464 Model 1: mu ~ 0 + isopto + fof_fiber + (1 | sessid)
1465 Model 2: mu ~ 0 + isopto + fof_fiber + isopto:fof_fiber + (1 | sessid)
1466     #Df LogLik Df Chisq Pr(>Chisq)
1467 1    3 -291.09
1468 2    4 -290.38  1 1.4303      0.2317

```

1469 1.3.4 Figure 6D, Right Panel, 2AFC task, Sham/FOF comparision

```

1470 Likelihood ratio test
1471
1472 Model 1: mu ~ 0 + isopto + fof_fiber + (1 | sessid)
1473 Model 2: mu ~ 0 + isopto + fof_fiber + isopto:fof_fiber + (1 | sessid)
1474     #Df LogLik Df Chisq Pr(>Chisq)
1475 1    3 -89.993
1476 2    4 -86.932  1 6.1215      0.01335 *
1477 ---
1478 Signif. codes:  0 '***' 0.001 '**' 0.01 '*' 0.05 '.' 0.1 ' ' 1

```

1479 1.3.5 Figure 6D, Main Comparision Between allo/2AFC task

```

1480 Likelihood ratio test
1481
1482 Model 1: mu ~ 0 + full_task + isopto + isopto:fof_fiber + isopto:fof_fiber:full_task +
1483           (1 | subjid/sessid)
1484 Model 2: mu ~ 0 + full_task + isopto + isopto:fof_fiber + isopto:fof_fiber +
1485           (1 | subjid/sessid)
1486     #Df LogLik Df Chisq Pr(>Chisq)
1487 1    6 -332.13
1488 2    5 -335.28 -1 6.2956      0.0121 *
1489 ---
1490 Signif. codes:  0 '***' 0.001 '**' 0.01 '*' 0.05 '.' 0.1 ' ' 1

```

1491 1.4 Supplementary Figure 5

1492 1.5 Supplementary Figure 5e

```

1493 [1] "Shapiro-Wilk test for ego group:"
1494
1495 Shapiro-Wilk normality test

```

```

1496
1497 data: df_ego$difference
1498 W = 0.94575, p-value = 0.1841
1499
1500 [1] "Shapiro-Wilk test for ego group:"
1501
1502 Shapiro-Wilk normality test
1503
1504 data: df_allo$difference
1505 W = 0.97455, p-value = 0.6878
1506
1507 [1] "Paired t-test for ego group:"
1508
1509 Paired t-test
1510
1511 data: df_ego$hit_rate_control and df_ego$hit_rate_cue
1512 t = 1.981, df = 25, p-value = 0.0587
1513 alternative hypothesis: true difference in means is not equal to 0
1514 95 percent confidence interval:
1515 -0.001837947 0.094502498
1516 sample estimates:
1517 mean of the differences
1518 0.04633228
1519
1520 [1] "Paired t-test for allo group:"
1521
1522 Paired t-test
1523
1524 data: df_allo$hit_rate_control and df_allo$hit_rate_cue
1525 t = 2.3504, df = 28, p-value = 0.02603
1526 alternative hypothesis: true difference in means is not equal to 0
1527 95 percent confidence interval:
1528 0.005109658 0.074424138
1529 sample estimates:
1530 mean of the differences
1531 0.0397669

```

1532 1.6 Supplementary Figure 5f

```

1533 [1] "Shapiro-Wilk test for ego group:"
1534
1535 Shapiro-Wilk normality test
1536
1537 data: df_ego$difference
1538 W = 0.96448, p-value = 0.4873
1539
1540 [1] "Shapiro-Wilk test for allo group:"
1541
1542 Shapiro-Wilk normality test

```

```

1543
1544 data: df_allo$difference
1545 W = 0.93863, p-value = 0.0923
1546
1547 [1] "Paired t-test for ego group:"
1548
1549 Paired t-test
1550
1551 data: df_ego$hit_rate_control and df_ego$hit_rate_delay
1552 t = 5.0063, df = 25, p-value = 3.667e-05
1553 alternative hypothesis: true difference in means is not equal to 0
1554 95 percent confidence interval:
1555 0.05423124 0.13003695
1556 sample estimates:
1557 mean of the differences
1558 0.09213409
1559
1560 [1] "Paired t-test for allo group:"
1561
1562 Paired t-test
1563
1564 data: df_allo$hit_rate_control and df_allo$hit_rate_delay
1565 t = 1.7685, df = 28, p-value = 0.08788
1566 alternative hypothesis: true difference in means is not equal to 0
1567 95 percent confidence interval:
1568 -0.004849284 0.066120464
1569 sample estimates:
1570 mean of the differences
1571 0.03063559

```

1572 1.7 Supplementary Figure 5g, Left Panel, Allo task, Sham/FOF com- 1573 parision

```

1574 Likelihood ratio test
1575
1576 Model 1: mu ~ 0 + isopto + fof_fiber + (1 | sessid)
1577 Model 2: mu ~ 0 + isopto + fof_fiber + isopto:fof_fiber + (1 | sessid)
1578 #Df LogLik Df Chisq Pr(>Chisq)
1579 1 3 -236.04
1580 2 4 -234.91 1 2.2586 0.1329

```

1581 1.8 Supplementary Figure 5g, Right Panel, Ego task, Sham/FOF com- 1582 parision

```

1583 Likelihood ratio test
1584
1585 Model 1: mu ~ 0 + isopto + fof_fiber + (1 | sessid)
1586 Model 2: mu ~ 0 + isopto + fof_fiber + isopto:fof_fiber + (1 | sessid)
1587 #Df LogLik Df Chisq Pr(>Chisq)

```

```

1588 1 3 -115.73
1589 2 4 -114.32 1 2.8171 0.09326 .
1590 ---
1591 Signif. codes: 0 '***' 0.001 '**' 0.01 '*' 0.05 '.' 0.1 ' ' 1

```

1592 1.8.1 Supplementary Figure 5g, Main Comparison Between allo/ego task

1593 Likelihood ratio test

```

1594
1595 Model 1: mu ~ 0 + ego_task + isopto + isopto:fof_fiber + isopto:fof_fiber:ego_task +
1596 (1 | sessid)
1597 Model 2: mu ~ 0 + ego_task + isopto + isopto:fof_fiber + (1 | sessid)
1598 #Df LogLik Df Chisq Pr(>Chisq)
1599 1 5 -358.34
1600 2 4 -358.35 -1 0.015 0.9025

```

1601 1.9 Supplementary Figure 5h, Left Panel, Allo task, Sham/FOF com- 1602 parision

1603 Likelihood ratio test

```

1604
1605 Model 1: mu ~ 0 + isopto + fof_fiber + (1 | sessid)
1606 Model 2: mu ~ 0 + isopto + fof_fiber + isopto:fof_fiber + (1 | sessid)
1607 #Df LogLik Df Chisq Pr(>Chisq)
1608 1 3 -238.48
1609 2 4 -238.01 1 0.9379 0.3328

```

1610 1.10 Supplementary Figure 5h, Right Panel, Ego task, Sham/FOF 1611 comparision

1612 Likelihood ratio test

```

1613
1614 Model 1: mu ~ 0 + isopto + fof_fiber + (1 | sessid)
1615 Model 2: mu ~ 0 + isopto + fof_fiber + isopto:fof_fiber + (1 | sessid)
1616 #Df LogLik Df Chisq Pr(>Chisq)
1617 1 3 -118.73
1618 2 4 -116.02 1 5.4103 0.02002 *
1619 ---
1620 Signif. codes: 0 '***' 0.001 '**' 0.01 '*' 0.05 '.' 0.1 ' ' 1

```

1621 1.10.1 Supplementary Figure 5h, Main Comparison Between allo/ego task

1622 Likelihood ratio test

```

1623
1624 Model 1: mu ~ 0 + ego_task + isopto + isopto:fof_fiber + isopto:fof_fiber:ego_task +
1625 (1 | sessid)
1626 Model 2: mu ~ 0 + ego_task + isopto + isopto:fof_fiber + (1 | sessid)
1627 #Df LogLik Df Chisq Pr(>Chisq)
1628 1 5 -363.23
1629 2 4 -365.27 -1 4.079 0.04342 *

```

```

1630 ---
1631 Signif. codes: 0 '***' 0.001 '**' 0.01 '*' 0.05 '.' 0.1 ' ' 1

1632 1.11 Supplementary Figure 6

1633 1.11.1 Supplementary Figure 6e, left Panel, Ego task, Sham/FOF compar-
1634 ision

1635 Likelihood ratio test
1636
1637 Model 1: mu ~ 0 + isopto + fof_fiber + (1 | sessid)
1638 Model 2: mu ~ 0 + isopto + fof_fiber + isopto:fof_fiber + (1 | sessid)
1639 #Df LogLik Df Chisq Pr(>Chisq)
1640 1 3 -571.04
1641 2 4 -530.34 1 81.403 < 2.2e-16 ***
1642
1643 1.11.2 Supplementary Figure 6e, right Panel, Allo task, Sham/FOF com-
1644 parision

1645 Likelihood ratio test
1646
1647 Model 1: mu ~ 0 + isopto + fof_fiber + (1 | sessid)
1648 Model 2: mu ~ 0 + isopto + fof_fiber + isopto:fof_fiber + (1 | sessid)
1649 #Df LogLik Df Chisq Pr(>Chisq)
1650 1 3 -477.31
1651 2 4 -477.25 1 0.1232 0.7256
1652
1653 1.11.3 Supplementary Figure 6f, left Panel, Ego task, Sham/FOF compar-
1654 ision

1655 Likelihood ratio test
1656
1657 Model 1: mu ~ 0 + isopto + fof_fiber + (1 | sessid)
1658 Model 2: mu ~ 0 + isopto + fof_fiber + isopto:fof_fiber + (1 | sessid)
1659 #Df LogLik Df Chisq Pr(>Chisq)
1660 1 3 -496.79
1661 2 4 -483.67 1 26.235 3.023e-07 ***
1662
1663 1.11.4 Supplementary Figure 6f, right Panel, Allo task, Sham/FOF com-
1664 parision

1665 Likelihood ratio test
1666
1667 Model 1: mu ~ 0 + isopto + fof_fiber + (1 | sessid)
1668 Model 2: mu ~ 0 + isopto + fof_fiber + isopto:fof_fiber + (1 | sessid)
1669 #Df LogLik Df Chisq Pr(>Chisq)
1670 1 3 -475.75
1671 2 4 -466.63 1 18.249 1.938e-05 ***
1672 ---
```

1672 Signif. codes: 0 ‘***’ 0.001 ‘**’ 0.01 ‘*’ 0.05 ‘.’ 0.1 ‘ ’ 1

Supplementary Table 2. $\Delta p(\text{Correct})$ and 95% C.I. between laser on/off trials for each rat on each experiment

task	laser epoch	subjID	region	n_trials(control)	$\Delta p(\text{Correct})$	95% C.I.	p-Val
allo	cue	JLI-R-0026	FOF	312(866)	-0.049516	[0.113069, 0.011119]	0.221140
			Sham	233(647)	-0.015860	[-0.089044, 0.055656]	0.761538
		JLI-R-0032	FOF	104(340)	-0.148998	[-0.257173, -0.041749]	0.011512(*)
			Sham	253(813)	-0.011448	[-0.078686, 0.058607]	0.955173
		JLI-R-0033	FOF	143(479)	-0.015701	[-0.102754, 0.073388]	0.714417
			Sham	300(1004)	-0.018699	[-0.078678, 0.041389]	0.727454
		JLI-R-0034	FOF	234(685)	-0.012718	[-0.088049, 0.063466]	0.901838
			Sham	320(989)	-0.032733	[-0.095131, 0.025790]	0.233662
		JLI-R-0036	FOF	209(709)	-0.023468	[-0.098372, 0.055393]	0.609981
			Sham	235(883)	0.009029	[-0.061000, 0.081170]	0.924860
	delay	JLI-R-0026	FOF	301(866)	-0.046011	[-0.110711, 0.018818]	0.250633
			Sham	234(647)	-0.071389	[-0.141296, 0.001482]	0.061751(.)
		JLI-R-0032	FOF	111(340)	-0.019925	[-0.122683, 0.083049]	0.883920
			Sham	251(813)	-0.002208	[-0.072446, 0.067380]	0.886522
		JLI-R-0033	FOF	169(479)	-0.049413	[-0.133725, 0.033767]	0.278868
			Sham	346(1004)	-0.044993	[-0.103051, 0.014320]	0.100101
		JLI-R-0034	FOF	248(685)	-0.021971	[-0.094171, 0.048545]	0.472752
			Sham	287(989)	0.019272	[-0.044661, 0.082145]	0.528069
		JLI-R-0036	FOF	218(709)	-0.015497	[-0.091778, 0.056947]	1.000000
			Sham	260(883)	-0.019940	[-0.089332, 0.048482]	0.406609
allo2AFC	cue	JLI-R-0026	FOF	77(184)	-0.018099	[-0.122681, 0.084177]	0.905438
			Sham	70(204)	0.042915	[-0.063032, 0.140240]	0.780706
		JLI-R-0034	FOF	78(242)	-0.044555	[-0.165318, 0.072558]	0.460535
			Sham	70(191)	0.015268	[-0.099314, 0.126261]	0.913880
		JLI-R-0036	FOF	62(233)	-0.045457	[-0.164811, 0.058616]	0.582136
			Sham	127(313)	0.023439	[-0.060807, 0.104975]	0.784986
	delay	JLI-R-0026	FOF	66(184)	-0.247064	[-0.385157, -0.111442]	0.000342(***)
			Sham	71(204)	-0.032731	[-0.153193, 0.082593]	0.763122
		JLI-R-0034	FOF	88(242)	-0.036953	[-0.148029, 0.070772]	0.619477
			Sham	73(191)	-0.008731	[-0.125786, 0.108667]	0.907986
		JLI-R-0036	FOF	85(233)	-0.113605	[-0.220949, -0.005856]	0.050654(.)
			Sham	123(313)	-0.009374	[-0.098751, 0.075917]	1.000000
ego	cue	JLI-R-0011	FOF	114(613)	-0.007365	[-0.108978, 0.100506]	0.893395
			Sham	191(761)	0.017805	[-0.064862, 0.093795]	1.000000
		JLI-R-0017	FOF	109(753)	-0.116380	[-0.220056, -0.016131]	0.006164(**)
			Sham	184(853)	-0.115612	[-0.203061, -0.033190]	0.011894(*)
		JLI-R-0020	FOF	269(892)	-0.041586	[-0.111688, 0.030269]	0.306069
			Sham	683(1869)	-0.014617	[-0.060357, 0.030059]	0.513458
		JLI-R-0022	FOF	139(727)	-0.028962	[-0.1116409, 0.060175]	0.438151
			Sham	356(1001)	0.037580	[-0.018565, 0.090620]	0.168160
	delay	JLI-R-0011	FOF	175(613)	-0.093055	[-0.173223, -0.011734]	0.039708(*)
			Sham	222(761)	0.005589	[-0.070261, 0.079575]	1.000000
		JLI-R-0017	FOF	178(753)	-0.106289	[-0.188384, -0.025089]	0.009753(**)
			Sham	205(853)	-0.063690	[-0.140026, 0.014211]	0.105367
		JLI-R-0020	FOF	317(892)	-0.107753	[-0.173502, -0.042469]	0.005681(**)
			Sham	677(1869)	-0.040938	[-0.085944, 0.004302]	0.048089(*)
		JLI-R-0022	FOF	219(727)	-0.072842	[-0.145957, -0.001361]	0.055825(.)
			Sham	362(1001)	-0.016802	[-0.075513, 0.039530]	0.557584

Supplementary Table 3. Effect size for $\Delta p(\text{correct})$ between laser on/off trials

Task	n_subj	Laser Period	Fiber Location	n_sess	n_trials(control)	effect size	95% C.I.	p-Val
allo	5	cue	FOF	29	1002(3079)	-0.040009	[-0.072301 -0.008449]	0.044528(*)
			Sham	40	1341(4336)	-0.014955	[-0.042427 0.014051]	0.044528(*)
	3	delay	FOF	29	1047(3079)	-0.030626	[-0.065043 0.002573]	0.213779(n.s.)
			Sham	40	1378(4336)	-0.020750	[-0.053316 0.011577]	0.213779(n.s.)
allo2AFC	3	cue	FOF	6	217(659)	-0.034630	[-0.064793 0.000592]	0.150659(n.s.)
			Sham	7	267(708)	0.026741	[-0.051375 0.113356]	0.150659(n.s.)
	4	delay	FOF	6	239(659)	-0.129968	[-0.215686 -0.053892]	0.013355(*)
			Sham	7	267(708)	-0.015447	[-0.033555 0.002500]	0.013355(*)
ego	4	cue	FOF	26	631(2985)	-0.046469	[-0.091577 -0.001443]	0.030966(*)
			Sham	35	1414(4484)	-0.007554	[-0.039761 0.026461]	0.030966(*)
	4	delay	FOF	26	889(2985)	-0.092011	[-0.127527 -0.056639]	0.002010(**)
			Sham	35	1466(4484)	-0.028008	[-0.057153 0.001234]	0.002010(**)